[redacted]

Center for Microgravity and Materials Research
The University of Alabama in Huntsville

FIFTH SEMI-ANNUAL PROGRESS REPORT

NASA GRANT NAG8-950

CONVECTIVE FLOW EFFECTS ON PROTEIN CRYSTAL GROWTH

Period of Performance
1/31/95 through 8/1/95

Principal Investigator
FRANZ ROSENBERGER

Center for Microgravity and Materials Research
University of Alabama in Huntsville
Huntsville, Alabama 35899

1. Introduction

During the fifth semi-annual period under this grant we have pursued the following activities:

- Characterization of the purity and further purification of lysozyme solutions: These efforts are summarized in Section 2.
- Crystal growth morphology and kinetics studies with tetragonal lysozyme: Our observations on the dependence of lysozyme growth kinetics on step sources and inpurities has been summarized in a manuscript which was accepted for publication in the Journal of Crystal Growth; see Attachment 1.
- Numerical modelling of the interaction between bulk transport and interface kinetics: For a detailed summary of this work see the manuscript (Attachment 2) which was accepted for publication in the Journal of Crystal Growth.
- Light scattering studies: This work has been summarized in a manuscript that has been submitted for publication to the Journal of Chemical Physics; see Attachment 3.

2. Protein characterization and purification

Since our crystal growth studies indicated the presence of impurities that impede step propagation on HEW lysozyme, we have systematically investigated the protein impurity contents of the stock material obtained from various suppliers. Two lysozyme materials were then further purified.

2.1. Protein impurity analyses

We have analyzed lysozyme (LYS) obtained from Sigma Chemical Company, Boehringer-Mannheim Corp. (BM) and Seikagaku America, Inc. (SK) for higher molecular weight protein impurities. The dissolution of these materials in buffer showed already significant differences. Sigma LYS was more difficult to dissolve and filter (0.45 μm). It was also turbid before filtering and upon standing for more than an hour at 5 °C a precipitate formed.

Electrophoretic analyses were performed with 12.5%T or 8-25%T SDS PAGE gels utilizing a silver staining system sensitive to 0.1 ng [X]. Sigma LYS contained four contaminating proteins. Their molecular weights M were determined by comparison with authentic protein standards. The band at M ≈ 18 kDa is suggestive of avidin that is present in egg white and has a monomeric M ≈ 18-19 kDa. However, immunoblotting indicated that this protein is *not* avidin. Sigma LYS also contained a M ≈ 28 kDa LYS dimer in SDS PAGE gels. The identity of this band was confirmed by binding a specific LYS antibody in immunoblotting (western blot). Two more contaminants were identified as ovalbumin (OVA, M ≈ 66 kDa) by immunoblotting and ovotransferrin (OVT, conalbumin, M ≈ 78 kDa) by its relative migration in

SDS gels compared to an authentic OVT standard. The protein identities of OVA and OVT were further supported by RP FPLC retention time data for the authentic standards and impurity peaks.

In order to determine the quantities of these contaminating proteins by scanning densitometry, we established concentration *vs.* optical density curves in SDS PAGE gels with authentic protein standards of OVT, OVA and LYS. For the evaluation of the unknown 18 kDa component, we assumed the same staining behavior as LYS. The results are summarized in Table 1. Based on this assumption, the total contaminating protein concentration in weight fractions were approximately: Sigma 5.7 %, Boehringer-Mannheim 3.8 %, and Seikagaku 1.5 %.

2.2. Lysozyme purification

Sigma LYS was purified by cation exchange Fast Protein Liquid Chromatography (CIE FPLC). Starting with 1 g of LYS, approximately 200 mg were recovered as electrophoretically pure as defined above. The CIE separation was isocratic in 10 mM CAPS buffer at pH = 10.4 with sodium chloride. A HiLoad semi-preparative CIE FPLC column yielded adequate resolution. All fractions were collected directly from the column in sodium acetate buffer to lower the pH to less than 7.0.

The purer SK LYS, when furtherpurified by the procedure used for Sigma LYS, retained significant impurity concentrations (mostly LYS dimer). Hence, a new procedure was developed using a pH gradient in 10 mM CAPS/sodium phosphate buffer. With a pH gradient from 10.4 to 12.0, the LYS could be purified with 30 %w recovery, however the sodium phosphate buffer complicated SDS PAGE purity determinations by causing LYS streaking. The same pH gradient in CAPS buffer alone and at low ionic strength caused precipitation of LYS near its isoelectric point. Use of 20 mM CAPS at pH = 11.0 with a sodium chloride gradient (0-200 mM in 1 hr) resulted in good separation. With significant ionic strength and a pH lower than the LYS pI, this procedure yields a soluble preparation with maximal recovery of approximately 50% of electrophoretically homogeneous LYS.

2.3. Conclusions

It is probable that all crystal growth and structure studies employing egg-white LYS have been contaminated by protein impurities on the order of 1-6%w and, hence, may not represent the intrinsic behavior of LYS. Future studies of LYS should be conducted with enzyme which has been demonstrably purified to the extent exhibited in this work or data should be given detailing why the high impurity levels of commercial LYS will not affect the results.

The formation of the LYS dimers, which appears to occur at high pH values, but not at typical crystal growth conditions (see Appendix 3) will be further investigated.

Reference

[1] J. Heukeshoven and R. Dernick, Electrophoresis 9 (1988) 28-32.

Table 1. Summary of Protein Impurities in Lysozyme

Contaminating Protein	**Sigma**	**BM**	**SK**
OVT (78 kDa)	0.2 %w 0.04 mol%	none detected	none detected
OVA (66 kDa)	3.8 %w 0.8 mol%	2.2 %w 0.5 mol%	none detected
LYS dimer (28 kDa)	0.7 %w 0.4 mol% monomer	0.45 %w 0.2 mol%	0.5 %w 0.3 mol%
Unknown (18 kDa)	1.0 %w as LYS 0.8 mol%	1.1 %w as LYS 0.8 mol%	1.0 %w as LYS 0.8 mol%
Total Contaminants	**5.7 %w** 2.0 mol%	**3.8 %w** 1.6 mol%	**1.5 %w** 1.1 mol%

CMMR MS 95-5 Accepted JCG July 1995

Dependence of lysozyme growth kinetics on step sources and impurities

Peter G. Vekilov and Franz Rosenberger

Center for Microgravity and Materials Research

University of Alabama in Huntsville, Huntsville, AL 35899, USA

Abstract

Interferometric microscopy was used to investigate the growth morphology and kinetics of {110} and {101} faces of tetragonal lysozyme crystals. Solutions were prepared from as-received Sigma and Seikagaku material, and Seikagaku lysozyme further purified by cation exchange liquid chromatography under salt-free conditions. The protein composition of the solutions was characterized by SDS electrophoresis with silver staining. We found that on crystals smaller than about 150 μm, 2D nucleation sites were randomly distributed over the faces. With increasing crystal size, surface nucleation predominantly occured at facet edges and, eventually, at facet corners. This reflects the higher interfacial supersaturation at these locations. However, on some crystals, we observed 2D nucleation at preferred non-corner sites presumably associated with defects. Upon abrupt temperature decreases, dislocation step sources formed on faces that previously had none. Within groups of dislocations, the dominating step source changed frequently. Depending on the activity of the dislocation groups, growth rates of different crystals differed by up to a factor of five during the same experiment. On facets with dislocation step sources, step generation by 2D nucleation became dominant above a critical supersaturation σ^*. In the absence of dislocations, nucleation-induced growth set in at $\sigma < \sigma^*$. In solutions with higher impurity concentrations, the density of the steps generated by 2D nucleation was higher *and* σ^* was lower. Hence, it appears that impurity adspecies are active in surface nucleation. The presence of less than 1 % of protein impurities with molecular weigtht (MW) ≥ 30 kD had significant effects on the crystallization kinetics. Step motion was impeded even at high σ, presumably through blocking of kink sites. In solutions without these high MW impurities, facets containing step sources did not grow below $\sigma = ln(C/C_{sat}) < 0.5$. In the less pure solutions such a "dead zone" was not observed. Hence, it appears that in lysozyme dead zones are caused by non-

protein impurities. In growth from the highly purified material no growth sector boundaries were visible, in contrast to the as-received lysozyme, and striae formation on growth temperature changes appeared drastically reduced.

1. Introduction

Lysozyme crystal growth has been investigated by standard [1-3] and interferometric optical microscopy [1,4-7], electron microscopy [8], atomic force microscopy (AFM)[9-11] and scanning tunneling microscopy [12]. These works showed that growth occurs through the spreading of steps generated by dislocations or 2D nuclei [4,5,8-12] and kinetics is influenced by the pH, precipitant concentration and impurities [1-5]. In this respect, as anticipated earlier [13,14], there appears to be no fundamental difference between the crystallization of (globular) proteins and small molecules [15].

Our recent high-resolution in-situ interferometry with digital signal processing [16,17], supported by numerical simulations of bulk transport [18] and its coupling to interface kinetics [19], has elucidated the dependence of the facet morphologies on the nonuniformities in solute and impurity supply. Fluctuations in the kinetics, that were briefly indicated in Ref. [16], and their possible role in lattice defect formation, will be dealt with in detail in Ref. [20]. The present paper deals with the *averaged* local normal growth rate, vicinal slope and tangential (step) velocity, and their dependence on supersaturation/temperature, layer source type and activity, and solution impurity content. Averaging was performed over the duration of several fluctuations, i.e. over periods of O(10 min). Both {110} and {101} faces were studied.

2. Experimental

The experimental procedures, solution preparation and the solubility data underlying the supersaturation values, $\sigma = ln[C/C_{sat}(T)]$, were as described earlier [1,16,21]. Solutions were prepared from hen-egg-white lysozyme supplied by Sigma Chemicals and Seikagaku Kogyo. In two sets of experiments, Sigma and Seikagaku materials were used as received. Electrophoretic (SDS-PAGE) analysis, using silver staining, revealed considerably larger concentrations of higher molecular weight (MW) impurities in Sigma stock than in Seikagaku lysozyme [17]. In addition,

we purified Seikagaku material by cation exchange under salt-free conditions, using a column equilibrated at pH = 4.5, and isocratic elution at pH = 9. As the comparison of the gels in Fig 1. shows, after this purification no higher MW protein impurities could be detected even on overloading with as much as 80 μg of protein per lane.

3. Morphology observations

3.1. Surface (2D) nucleation

Fig. 2 shows the development of the morphology of a (101) face with crystal size and supersaturation during growth from a Sigma solution. On the small crystal (Fig. 2a), interferometric intensity changes occurred uniformly across the facet, and growth was observed only at $\sigma > 1.3$ (see Sect. 4.1.). Hence, we conclude that growth steps were generated by randomly distributed 2D nucleation, in agreement with earlier electron microscopy and AFM observations with lysozyme [8,9]. With increase in supersaturation/growth-rate and facet size, layer generation preferentially occurred along the crystal edges. The specific nucleation sites moved with time; compare Figs. 2b and 2c. With further increase of facet size and σ, the steps were predominantly generated at the facet corners; Fig. 2d. We observed this trend in numerous experiments with {101}and {110} faces growing from Sigma as well as the purer Seikagaku solutions. This transition in nucleation locations reflects the increase in σ-nonuniformity with crystal size and growth rate [18,19,22,23].

In a few observations, however, steps persistently originated at locations near corners or edges even at small crystal sizes, or low growth rates; see e.g. the frame sequence of Fig. 4 in Ref. [17]. Yet, these crystals did not grow at $\sigma \leq 1.6$. Thus, apparently no active dislocation step-sources were present, and the pinning of the step generation locations was probably due to other lattice defects [24-26] that can locally enhance 2D nucleation [26-29].

3.2. Dislocation step sources

In a (110) growth experiment with a Sigma solution, we first lowered the supersaturation in six steps from $\sigma = 1.13$ to $\sigma = 0.26$, and then raised it to 1.38 in four steps over a total period of about 30 hours. The interferograms of Fig. 3 present selected morphology responses to these

σ-changes. The four growth hillocks that sequentially dominated the facet morphology (Figs. 3a - 3d) remained at their respective positions throughout two or three supersaturation steps, during which the crystal grew from ~1.5 to ~2 μm per step. Note that these hillock are not positioned at the edges, where the higher σ [18,22,23] favors 2D nucleation. Thus, we conclude that the hillocks represent dislocation growth spirals [8,9,30]. The change of the leading hillock is due to the fact that, at the altered conditions, the new hillock provides a faster growth rate than the old one. Only growth hillocks of equal activity can maintain coexistence on a facet.

Similar changes of the leading dislocation source have been observed in inorganic crystals [31-33] and have been interpreted in terms of complex dislocation sources, consisting of several dislocations [30]. In inorganic systems, the dislocation sources' interplay is usually reversible: changing σ to a previous value leads to the reemergence of the hillock that previously dominated under this condition [32]. For our system, as reflected by Figs. 3a and 3d, this was apparently not the case. Furthermore, in inorganic crystals the new dislocation step source usually possesses higher activity as manifested by a higher hillock slope. Comparing, for instance, Figs. 3a and 3b we see that in our system the new hillock slope is much *lower* than the slope of the previously existing one. Assuming that the slope is not affected by impurities, and increases at most linearly with σ [30,31,34] this difference cannot be accounted for by the lower supersaturation. Yet, this behavior can be explained if we assume that, in contrast to inorganic crystals [32], the distance between the dislocations constituting the growth sources in Fig. 3, varies. Then, increase in the distance between dislocations in the old growth source will lead to a drop of activity [30-32], whence even a dislocation group with a lower original activity can dominate the facet. This apparent mobility of the dislocation lines in lysozyme is probably related to the substantially lower unresolved critical shear stress in protein crystals.

On renewed increase in σ, in analogy to the (101) face of Fig. 2d, step generation was localized to the upper right and lower left corner of the facet in Figs. 3d and 3e, respectively. While the dislocations' activity in step generation increases less than linearly with σ [31,34], the

activity of 2D nucleation is an exponential function of σ [35,36]. Hence, as shown by Fig. 3e, at higher supersaturations 2D nucleation became the dominating layer generation mechanism.

3.3. Creation of dislocation step sources

In another (110) growth experiment from a Seikagaku solution, initially no dislocation step-sources were apparent. Similar to the (101) face of Fig. 2a, we see in Fig. 4a that at smaller crystal size and growth rate (see Sect. 4.3.), the facet was flat, indicating growth by uniformly distributed 2D nuclei. The higher growth rate at higher σ in Fig. 4b results, again similar to Fig. 2, in dominance of the nucleation along the facet edges.

Next, using a ramp rate of 0.5 °C/min, we lowered the temperature from 19 °C (σ = 1.80) to 12 °C (σ = 2.84) for 3 hours and then to 10 °C (σ = 3.22) for about 4 hours. Then T was again increased to 20 °C (σ = 1.64). The facet morphology remained essentially the same as in Fig. 4b. The only effect of these sharp supersaturation changes seemed to be the appearance of a second crystal on top of the first one. No interference fringes appeared on its top face. Hence, the new crystal was substantially misoriented with respect to the first one, and, thus, no steps originated from the reentrant angle between the two crystals. The new crystal grew much more rapidly than the first one, even at low σ, as can be seen from their relative change in lateral dimensions in Figs. 4c - 4f. Thus we see that two crystals can grow with greatly differing rates under identical solution conditions. From this difference in growth rate, and since the new crystal nucleated at lower T and higher σ, we speculate that it possesses a substantially higher defect density than the first crystal.

After overnight growth at σ = 1.64, a hillock was observed at the lower left part of the facet of the first crystal, Fig. 4c. Since this hillock existed for about a day, in which the studied face grew about 13 μm, it probably indicates outcropping dislocations at this face location. Then, the facet became covered by steps coming from the steeper hillocks depicted in Fig. 4d. The supersaturation was kept constant for several hours, during which the top face grew by about 4 μm and the growth hillock became much steeper, Fig. 4e. After an another overnight growth at σ = 0.83, the hillock's steepness increased further, Fig. 3f, in spite of the lower supersaturation. On

further decrease of σ to 0.55, the hillock slope remained practically unchanged; see Sect 4.3 for kinetics details.

The continuing increase of the hillock slope at constant or decreasing σ can be explained as follows. The dislocation groups active in Figs. 4c - 4f have probably formed in response to the drastic temperature lowering/supersaturation increases, likely by the trapping of a foreign particle or a drop of mother liquor [37]. Since initially no growth activity resulted, the group must have had a practically zero net Burgers vector, combined with a large circumference of the created dislocation bunch [30-32]. Closely packed dislocations tend to diverge during growth since this decreases the elastic energy of the group [38]. When the distance between any pair of neighboring dislocations reaches about 10 critical 2D-nucleus radii [30,39,40], one (or more) dislocation group(s) will start generating growth steps, provided that it has a shorter circumference and greater net Burgers vector. Further, as the dislocations continue to fan out, their activity will increase. If several of the secondary (or tertiary,...) bunches attain growth activity, they will compete, similar to the observations in Sect. 3.2. This may lead to the changing growth hillocks pattern in Figs. 4d - 4f.

4. Kinetics measurements

4.1. (101) face growth from Sigma solution: 2D nucleation step sources

Fig. 5 presents the dependencies of the normal growth rate R, local slope p and tangential (step) velocity v on supersaturation at a center and edge location of Fig. 2. For comparison, we have also plotted some $R(\sigma)$ and $v(\sigma)$ data from our previous measurements [1,4,5]. We see that in the current case, growth started at a considerably higher $\sigma \approx 1.4$. This is probably due to the presence of dislocation step sources in the earlier experiments, while Fig. 2 clearly indicated growth step generation by 2D nucleation only. Note also that at $\sigma \geq 2.5$ ($T \leq 14^{o}$C), $p(\sigma)$ rises less rapidly than in the lower supersaturation range. This is most likely due to reduced layer generation at the lower temperatures. The lower slope at the facet center than at the periphery, Fig. 5b, was related to nonuniform surface impurity concentration, see details in Refs. [17,19].

The tangential velocity, Fig. 5c, is very low at $\sigma < 1.5$, but sharply accelerates at slightly higher σ. This indicates the strong action of step blocking [41-43] impurities at low growth rates. As R sharply increases due to the fast increase in p, the exposure time of the crystal surface between the passing of steps decreases [44-46]. This leads to lower impurity surface concentrations, weaker impurity action, and thus to a steep rise in $v(\sigma)$. We have observed similar effects for dislocation-generated growth, where the much weaker $p(\sigma)$ dependence resulted in a less pronounced rise in $R(\sigma)$ [4,5].

At $\sigma \geq 2.4$, v *decreases* with increasing supersaturation. Such deceleration of v has not been observed before, neither in protein nor in small molecule crystal growth. Several mechanisms, or a combination of them, could be responsible for the observed effect. It could be related to the decreasing temperature through the activation energies of the incorporation processes. Further, since adsorption is always exothermic and thus enhanced by lower temperatures, the quantity of impurity adspecies may increase. Another cause, in analogy to inorganic crystals [32], may be a variation in the step patterns generated by 2D nucleation. In addition, the decreasing $v(\sigma)$ could be due to overlapping of the step (bulk [30,47] or surface [30,48,49]) diffusion fields with the higher p. Evidence for the participation of surface diffusion in the incorporation process comes form the strong coupling between fluctuations of the local slope and tangential velocity [20], and from the response of the surface morphology to σ-nonuniformity [17].

Another possibility for a decrease in v at high σ/low T is a change in the lysozyme species in the solution. This may either be a conformational modification, or a change in the aggregate state of lysozyme molecules [3,50,51]. This, however, should also be reflected in the $v(\sigma)$ of the {110} faces, which, as we will see below, is not the case. For further evidence for the absence of equilibrium aggregates in lysozyme solutions see Ref. [52].

From the above we can conclude that the non-monotonic behavior of R at $\sigma \geq 3$ is due to the opposite nonlinear changes in p and v at these supersaturations.

4.2. (110) face growth from Sigma solution: dislocation step sources

Fig. 6 presents kinetics data for the face depicted in Fig. 3, together with high-σ results obtained on another crystal whose morphological evolution was presented in Fig. 7 of Ref. [17]. Based on the morphology observations of Fig. 3, we concluded that, at low σ-s, growth steps were generated by different dislocation groups with varying activity. This is also reflected in the non-monotonic behavior of $p(\sigma)$ for $\sigma < 1$, Fig. 6b. At low σ, in the impurity influenced region, higher p leads to *greater* v. Similar behavior has been observed in the same σ-range on the (101) lysozyme face [5], and has been attributed to time-dependent impurity adsorption, see also the discussion in Sect. 4.1.

In the high supersaturation region ($\sigma > 1.3$), we observed 2D nucleation localized at the outcrops of lattice defects as described in Sect 3.1. We speculate that the decrease in the step generation activity at higher σ, leading to lower p, is due to some growth-induced spatial rearrangement of the defects. The great differences in p and v measured at the facet periphery and center at $\sigma > 1.5$ are due to solute and impurities nonuniformities and are discussed in detail in Ref. [17]. In this σ region, a decrease in p leads to an *increase* in v. This indicates strong overlapping of step (surface) diffusion fields for this face, as discussed in Ref. [17].

For $1.4 < \sigma < 2.1$, v at the facet edge increases roughly linearly with supersaturation. This permits for a simple evaluation of effective step kinetics coefficients. Using the common definitions

$$v = b_{step}\,\sigma = \beta_{step}\Omega\, C\,\sigma \quad , \tag{1}$$

we obtain $b_{step} = 8\times10^{-6}$ cm/s, $\beta_{step} = 1.4\times10^{-4}$ cm/s. In (1), the product ΩC accounts for the change in mass density during crystallization, and $\Omega = 3\times10^{-20}$ cm^3 is the volume per lysozyme molecule in the crystal. Comparing the b_{step} value to the one in the purer, Seikagaku solutions, Sect. 4.3, we see that it is much lower in the Sigma solution. This means that some of the impurities present in the system, see Sect. 2, are active even at high supersaturations. This conclusion is in agreement with our observations of impurity influence on microscopic growth morphology [17], that show strong impurity effects in the same supersaturation range. The fact

that, in spite of the impurity action, v increases roughly linearly with σ, could indicate impurity action by partial blocking of kink sites at the steps [53], in agreement with our assumptions made in Refs. [17,19] to quantitatively account for the observed vicinal slope distributions across facets.

The R-data for $\sigma > 2$ in Fig. 6a, strongly deviate from our earlier measurements in which R increased with σ up to $\sigma \approx 3$. Contrary to the above observation for the (101) face in the same solution, the $v(110)$ at the facet edge, where the steps are generated, increased monotonically with σ, Fig. 6c. Thus the reason for much lower R values, and for the decrease of R with σ in the present experiment is the drop in step generation activity, indicated by the $p(\sigma)$ at high supersaturation; Fig. 6b.

4.3. (110) face growth from Seikagaku solution

The dependencies of R, p and v on the supersaturation for this case are depicted in Fig. 7. The measurements were performed on two crystals, in two different experiments: the morphology of the first is shown in Fig. 4, and of the second, in Fig. 4 of Ref. [17].

In the 2D nucleation dominated region, the local slope, Fig. 7b, did not differ for the two crystals. It was up to 2-3 times lower than for growth from Sigma solutions in Fig. 6. Moreover, if no active dislocations outcropped on the studied face, 2D nucleation activity became significant only at $\sigma > 1.8$. This is much higher than for the Sigma solutions, where growth by 2D nucleation consistently started at $\sigma \approx 1.1$ - 1.3. These two facts may indicate the participation of the protein impurities in the processes of surface nucleation, similar to deductions for dislocation-free (101) ADP faces [54].

Fig. 7c shows that at $\sigma < 0.5$, v is practically zero, the crystal does not grow although dislocation step sources are available. Comparing this to the $v(\sigma)$ in Fig. 6c, we see that in the Sigma solution the "dead zone" is narrower, or even absent. The same dependence of the "dead zone" width on the source material was observed on the (101) lysozyme face [5]. Since now we know that Sigma lysozyme contains *higher* amounts of protein impurities, we can speculate that the "dead zone" at low σ is caused by non-protein foreign species.

Between $0.5 < \sigma < 2.3$, v sharply accelerates. Since this is accompanied by a fast increase in R, we can associate it with the shortening of the exposure times of the terraces between the passing of steps as the growth rate increases [5,44-46], see Sect. 3.1. At $\sigma > 2.3$ the tangential velocity is a roughly linear function of supersaturation. This allows us again to determine the two step kinetic coefficients, as defined in Sect. 4.2: $b_{step} = 1.2\times10^{-5}$ cm/s, $\beta_{step} = 2.3\times10^{-4}$ cm/s. The difference between v at edge and center, when the facet width is > 200 μm, is discussed in Ref. [17].

4.4. Growth from purified solution

The (110) tangential velocity obtained on growth fronts of comparable average slope with the three types of solutions are compared in Fig. 8. In the experiment with purified lysozyme, no dislocations outcropped on the studied face. Accordingly, the crystal grew only at $\sigma > 1.4$ by 2D nucleation. However, in contrast to the less pure cases (see also Sect. 4.1.), there was no region of rapid non-linear increase in $v(\sigma)$. We see that with the purified lysozyme, v is faster than in Sigma and Seikagaku solutions. Since they were obtained with comparable slope (step density), these differences in kinetics are likely due to impurity action even at high supersaturations. The step kinetics coefficients, defined by Eq. (1), are $b_{step} = 1.7\times10^{-5}$ cm/s and $\beta_{step} = 3.6\times10^{-4}$ cm/s. For the (101) face $\beta_{step} = 2.8\times10^{-4}$ cm/s [4,5]. This may be why at high σ, where impurity effects are weaker, the (110) face grows faster and the crystals are more isometric. At low supersaturations, impurities have a stronger effect on the (110) face, the (101) face grows faster, and the crystals become elongated in the z-direction.

To assess possible effects of solution purity on crystal quality, we used differential interference contrast microscopy to compare two crystals grown from the less pure Sigma and the purified solution, respectively. During the growth, the temperature was changed in 1 °C steps for the first crystal, and in 2, 6 and 12 °C steps for the second. In spite of these drastic changes, we see that the resulting striations [1] are substantially weaker for the purer solution. Further, no boundaries between the (110) and (101) growth sectors are visible in the second crystal. Thus, high purity of the source material is highly beneficial for the quality of the grown crystals.

5. Conclusions

We have investigated the growth morphology and kinetics of tetragonal lysozyme crystals in unstirred solutions with characterized protein composition. We have shown that the presence of less than 1% of high MW protein impurities strongly affects growth kinetics and degrades the compositional uniformity of the crystals.

In the absence of dislocations cropping out on a face, the crystals did not grow at supersaturations below a threshold of 1.1 - 1.8 for both {110} and {101} faces. At high supersaturations, growth layers were always generated by 2D nucleation. The threshold supersaturation for growth by this mechanism increased with higher solution purity. 2D nucleation occurred uniformly over the facet under conditions where supersaturation gradients were insignificant. Larger crystal sizes and higher growth rates resulted in localization of 2D nucleation to facet edges and corners, where the supersaturation is higher. On some crystals, 2D nucleation always occurred at preferred non-corner sites, presumably at outcrops of structural defects.

In the supersaturation range in which growth steps are generated by dislocations, the normal growth rate varied, presumably due to changing activity of the dislocation sources. This was accompanied by frequent changes of the specific step generators that dominated the growth morphology. Since in some occasions the victorious source possessed weaker activity than the previously dominating one, we interpret these transitions in terms of spatial rearrangements of the dislocations within the respective sources. By rapid dropping of the growth temperature, we were able to induce dislocation growth step source on a crystal that previously had none. The activity of this dislocation group increased at constant conditions, presumably because the constituent dislocations attained divergent orientations to lessen the elastic energy of the group.

Protein impurities affect growth kinetics by slowing down step propagation in the whole range of supersaturations investigated. A dead zone at $\sigma < 0.5$ was present in growth from purer solutions and, thus, is likely due to non-protein impurities. The growth rate of a (101) face changed non-monotonically with supersaturation at $\sigma > 2.8$ ($T < 12$ °C). Enhanced impurity adsorption at this low temperature is the most probable cause. In solutions that did not contain

these impurities, the density of steps generated by 2D nucleation was lower. This, and the increase in the threshold supersaturation for 2D nucleation, make us believe that the impurity adspecies on the interface facilitate surface nucleation.

Acknowledgments

Support for this work by NASA (Grant # NAG8-950), NSF (Grant # DMB-9104630) and the State of Alabama through the Center for Microgravity and Materials Research at the University of Alabama in Huntsville, is gratefully acknowledged. We also thank Mary Alpaugh for the protein purification and analyses, and Lynne Carver for preparing the figures.

References

1. L.A. Monaco and F. Rosenberger, J. Crystal Growth 129 (1993) 465.
2. E. Forsythe and M.L Pusey, J. Crystal Growth 139 (1994) 89.
3. M.L. Pusey, J. Crystal Growth 122 (1992) 1.
4. P.G. Vekilov, M. Ataka and T. Katsura, J. Crystal Growth 130 (1993) 317.
5. P.G. Vekilov, M. Ataka and T. Katsura, Acta Crystallogr. D 51 (1995) 207; P.G. Vekilov, Prog. Crystal Growth and Charact. 26 (1993) 25.
6. H. Komatsu, S. Miyashita and Y. Suzuki, Jpn. J. Appl. Phys 32 (1993) 1855.
7. S. Miyashita, H. Komatsu, Y. Suzuki and T. Nakada, J. Crystal Growth 141 (1994) 419.
8. S.D. Durbin and G. Feher, J. Mol. Biol. 212 (1990) 763.
9. S.D. Durbin and W.E. Carson, J. Crystal Growth 122 (1992) 71.
10. S.D. Durbin, W.E. Carson and M.T. Saros, J. Phys. D: Appl. Phys. 26 (1993) B128.
11. J.H. Konnert, P. D'Antonio and K.B. Ward, Acta Cryst. D50 (1994) 603.
12. W. Littke, M. Haber and H.-J. Güntherodt, J. Crystal Growth 122 (1992) 80.
13. F. Rosenberger, J. Crystal Growth 76 (1986) 618.
14. R.S. Feigelson, J. Crystal Growth 90 (1988) 1.
15. R. Giegé, B. Lorber and A. Théobald-Dietrich, Acta Crystallogr. D 50 (1994) 339.
16. P.G. Vekilov, L.A. Monaco and F. Rosenberger, J. Crystal Growth 148 (1995) 289.

17. P.G. Vekilov, L.A. Monaco and F. Rosenberger, J. Crystal Growth, in press.

18. H. Lin, F. Rosenberger, J.I.D. Alexander and A. Nadarajah, J. Crystal Growth 151 (1995) 153.

19. H. Lin, P.G. Vekilov and F. Rosenberger, J. Crystal Growth, submitted.

20. P.G. Vekilov and F. Rosenberger, in preparation

21. F. Rosenberger, S.B. Howard, J.W. Sowers and T.A. Nyce, J. Crystal Growth 129 (1993) 1.

22. A. Seeger, Phil. Mag. 44 (1953) 348.

23. W.R. Wilcox, J. Crystal Growth 37 (1977) 229.

24. E. Bauser and H. Strunk, J. Crystal Growth 51 (1981) 362.

25. J.N. Sherwood and T. Shripathi, J. Crystal Growth 88 (1988) 358.

26. J.N. Sherwood and T. Shripathi, Faraday Discuss. 95 (1993) 173.

27. F.C. Frank, J. Crystal Growth 51 (1981) 367.

28. L.J. Gillig and B. Dam, J. Crystal Growth 67 (1984) 400.

29. General Discussion, Faraday Discuss. 95 (1993) 253.

30. W.K. Burton, N. Cabrera and F.C. Frank, Phil. Trans. Roy. Soc. London A243 (1951) 299.

31. A.A. Chernov, L.N. Rashkovich and A.A. Mkrtchan, J. Crystal Growth 74 (1986) 101.

32. P.G. Vekilov and Yu.G. Kuznetsov, J. Crystal Growth 119 (1992) 248.

33. K. Maiwa, K. Tsukamoto and I. Sunagawa, J. Crystal Growth 102 (1990) 43.

34. P.G. Vekilov, Yu.G. Kuznetsov and A.A. Chernov, J. Crystal Growth 121 (1992) 643.

35. J.D. Weeks and G.H. Gilmer, Advan. Chem. Phys. 40 (1979) 157.

36. W. Obretenov, D. Kashchiev and V. Bostanov, J. Crystal Growth 96 (1989) 843.

37. A.A. Chernov, Modern Crystallography III, Growth of Crystals (Springer, Berlin, 1984) p. 256.

38. M.C. Meyers and K.K. Chawla, Mechanical Metallurgy (Prentice Hall, Eaglewood Cliffs, 1984) p. 359.

39. N. Cabrera and M. Levine, Phil. Mag. 1 (1956) 450.

40. B. van der Hoek, J.P. van der Eerden and P. Benema, J. Crystal Growth 56 (1982) 621.

41. N. Cabrera and D.A. Vermileya, in: Growth and Perfection of Crystals, Eds. R.H. Doremus, B.W. Roberts and D. Turnbull (Wiley, New York, 1958) p. 393.

42. V.V. Voronkov and L.N. Rashkovich, Soviet Phys. - Crystallogr. 37 (1992) 289.

43. V.V. Voronkov and L.N. Rashkovich, J. Crystal Growth 144 (1994) 107.

44. A.A. Chernov, V.F. Parvov, M.O. Kliya, D.V. Kostomarov and Yu.G. Kuznetsov, Soviet Phys. - Crystallogr. 26 (1981) 640.

45. A.A. Chernov and L.N. Rashkovich, J. Crystal Growth 84 (1987) 389.

46. A.A. Chernov and A.J. Malkin, J. Crystal Growth 92 (1988) 432.

47. A.A. Chernov, Soviet Phys. - Uspekhi 4 (1961) 116.

48. G.H. Gilmer, R. Ghez and N. Cabrera, J. Crystal Growth 8 (1971) 79.

49. J.P. van der Eerden, J. Crystal Growth 56 (1982) 174.

50. L.J. Wilson and M.L Pusey, J. Crystal Growth 122 (1992) 8.

51. M.L. Pusey, private communication.

52. M.Muschol and F. Rosenberger, in preparation.

53. Ref. [36], p. 161.

54. A.J. Malkin, A.A. Chernov and I.V. Alexeev, J. Crystal Growth 97 (1989) 765.

Figure captions

Fig. 1. Protein composition of hen-egg-white lysozyme solutions prepared from Sigma, Seikagaku and purified Seikagaku stock. Sodium dodecyl sulfate polyacrilamide gel electrophoresis (SDS PAGE) with silver staining. Protein loads indicated for each lane.

Fig. 2. Development of the growth morphology on a (101) face of a tetragonal lysozyme crystal, with no active dislocation step sources, growing from a Sigma solution. Twenty minutes elapsed between (b) and (c). Supersaturations indicated for each frame.

Fig. 3. Development of the growth morphology on a (110) face of a tetragonal lysozyme crystal, with several dislocation step sources with varying activity, growing from a Sigma solution.

Fig. 4. Development of the growth morphology on a (110) face of a tetragonal lysozyme crystal, growing from a Seikagaku solution. Between (b) and (c) the supersaturation was temporarily increased to 2.84 and 3.22 (see text), resulting in the dislocation step sources seen in (c) - (f).

Fig. 5. Dependencies of (a) the normal growth rate R, (b) local slope p and (c) tangential velocity v, on the supersaturation σ, measured at two positions on a (101) face of a crystal growing from a Sigma solution.

Fig. 6. Dependencies of (a) the normal growth rate R, (b) local slope p and (c) tangential velocity v, on the supersaturation σ, measured at three positions on a (110) face of a crystal growing from a Sigma solution. Arrows indicate sequence of σ-changes.

Fig. 7. Dependencies of (a) the normal growth rate R, (b) local slope p and (c) tangential velocity v, on the supersaturation σ, measured at two positions on a (110) face of a crystal growing from a Seikagaku solution. Arrows indicate crystal size increase.

Fig. 8. Dependencies of the tangential velocity v on the supersaturation σ, measured at the edges of (110) faces of crystals growing from Sigma, Seikagaku and purified solutions. The respective slopes for the Sigma and Seikagaku runs are shown in Figs. 6b and 7b. For the purified solution data, $3\times10^{-3} < p(\sigma) < 6\times10^{-3}$.

Fig. 9. Comparison of the quality of crystals grown from (a) Sigma and (b) purified lysozyme solutions. Differential interference contrast microscopy images. Temperature steps to induce inhomogeneities indicated in each frame. Growth from purer solution results in much weaker striation formation in response to (larger) temperature/supersaturation changes and absence of growth sector boundaries. Note that the focal plane is in the interior of the crystals; hence, the edges of the larger crystal in (b) appear more blurred.

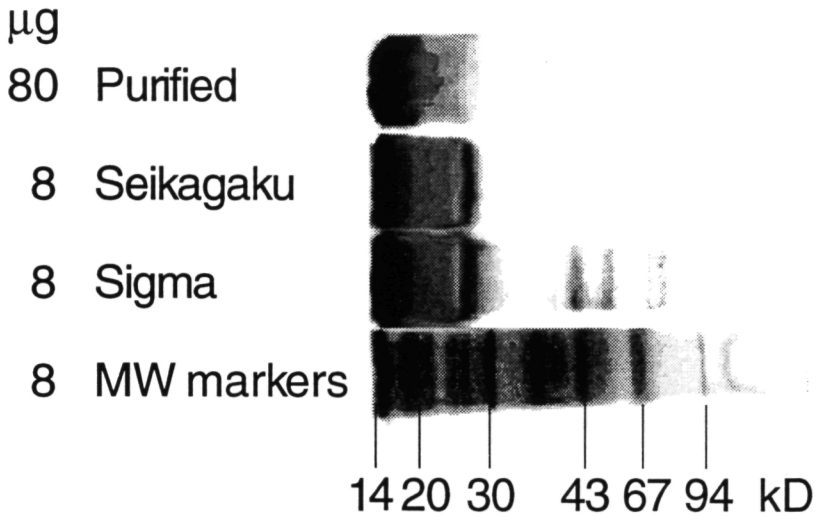
µg
80 Purified
8 Seikagaku
8 Sigma
8 MW markers
14 20 30 43 67 94 kD

FIG. 1

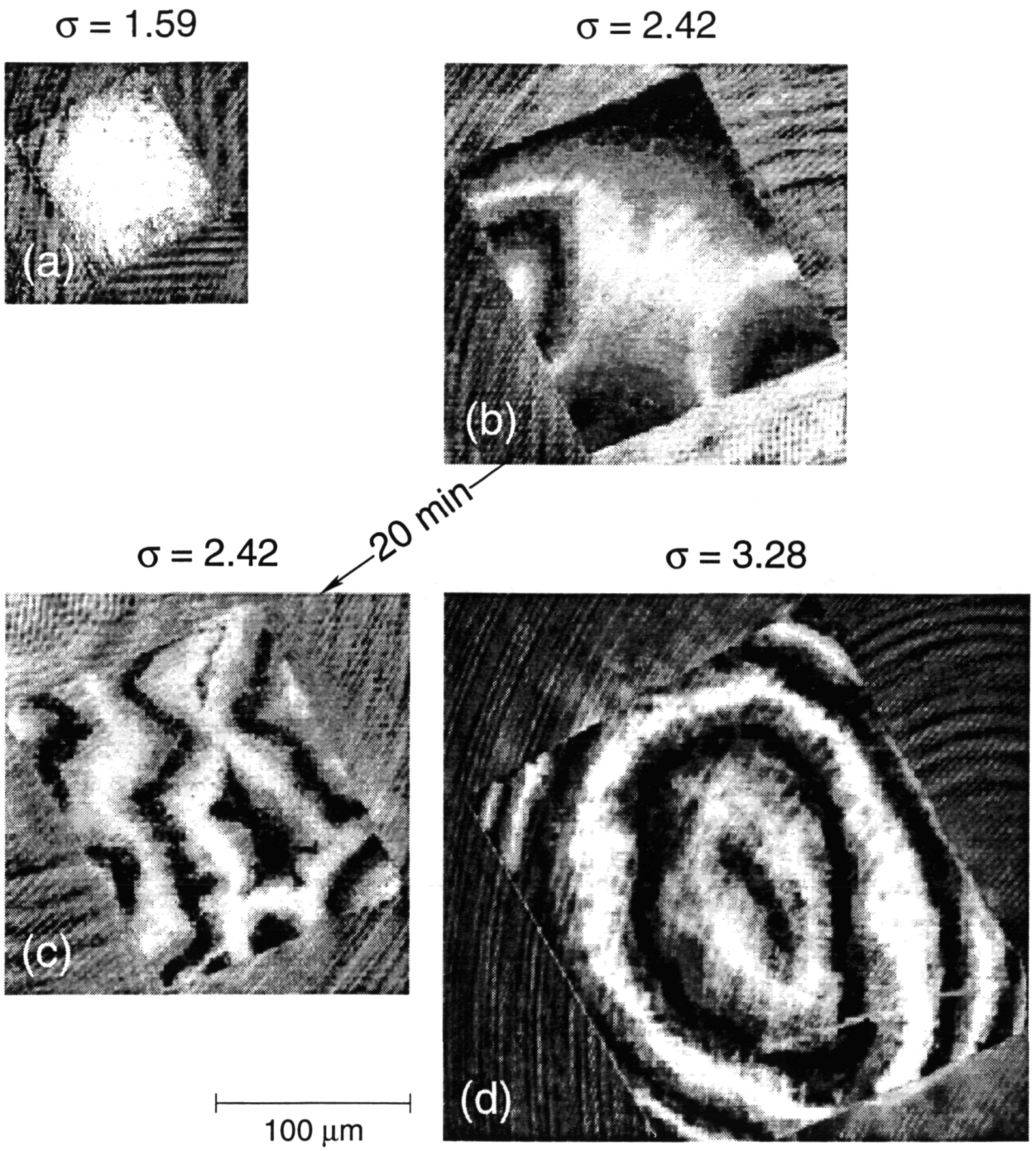

FIG. 2

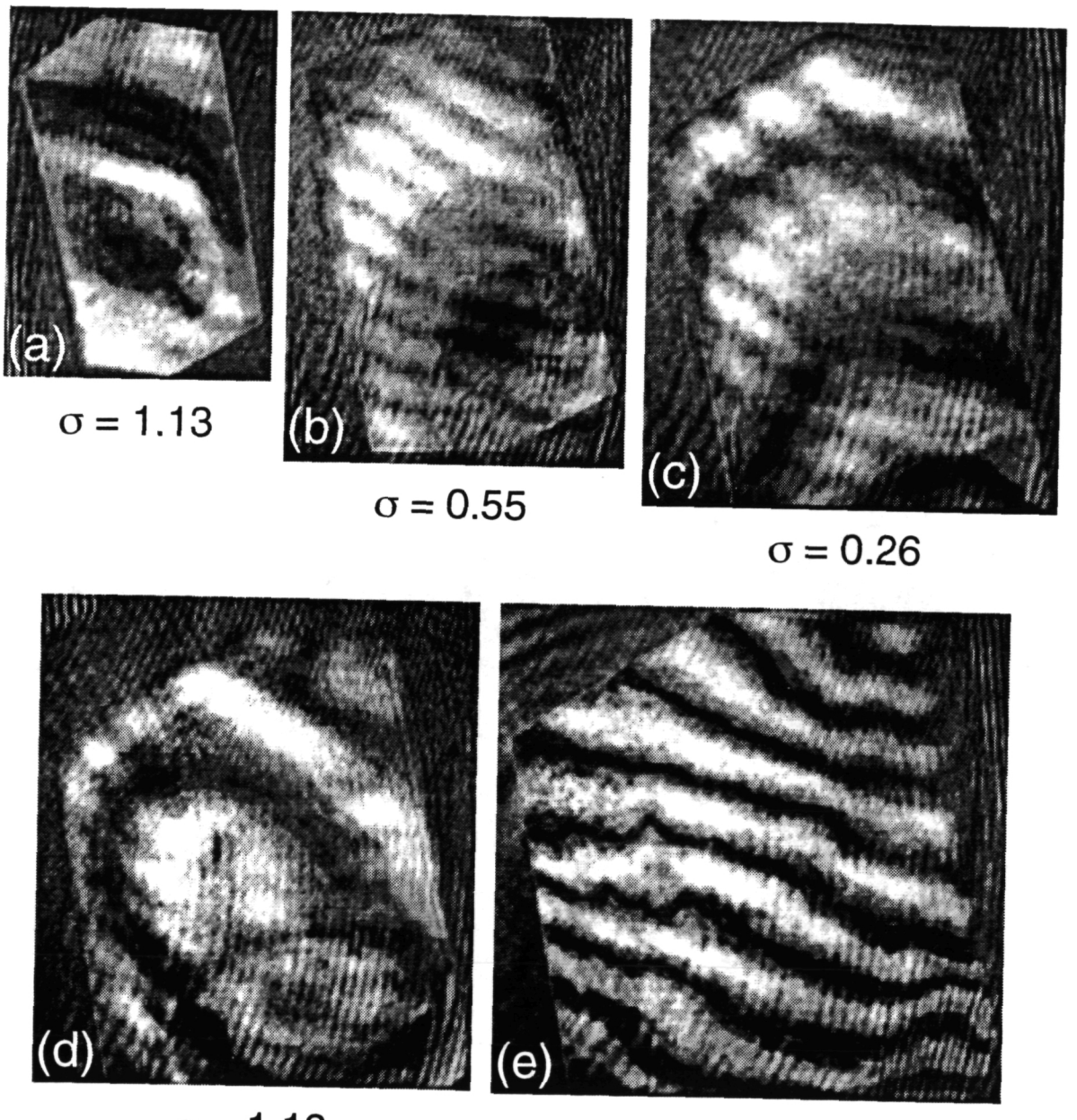

FIG. 3

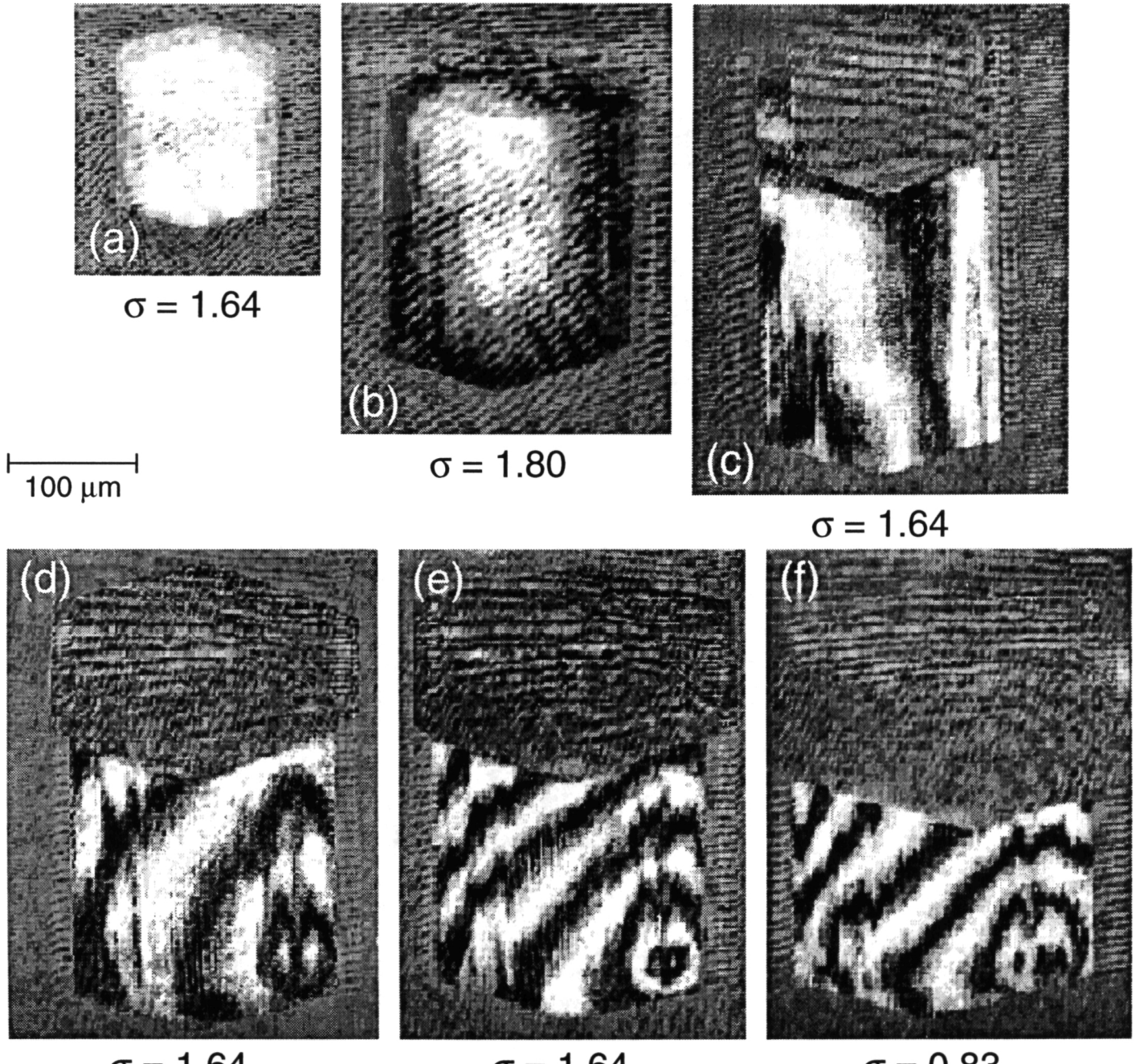

FIG. 4

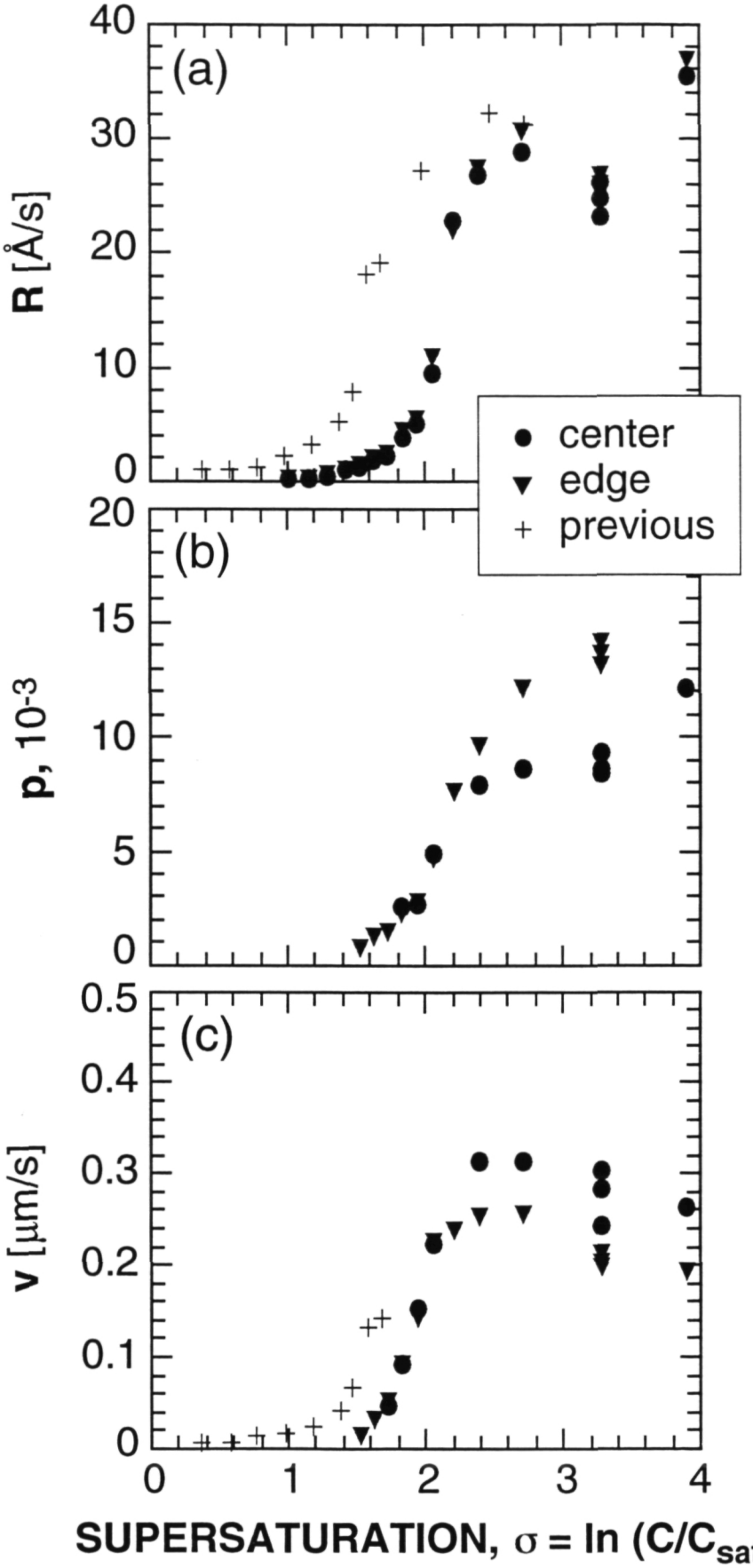
(a)
(b)
(c)
R [Å/s]
p, 10-3
v [μm/s]
center
edge
previous
SUPERSATURATION, σ = ln (C/Csat)

FIG. 5

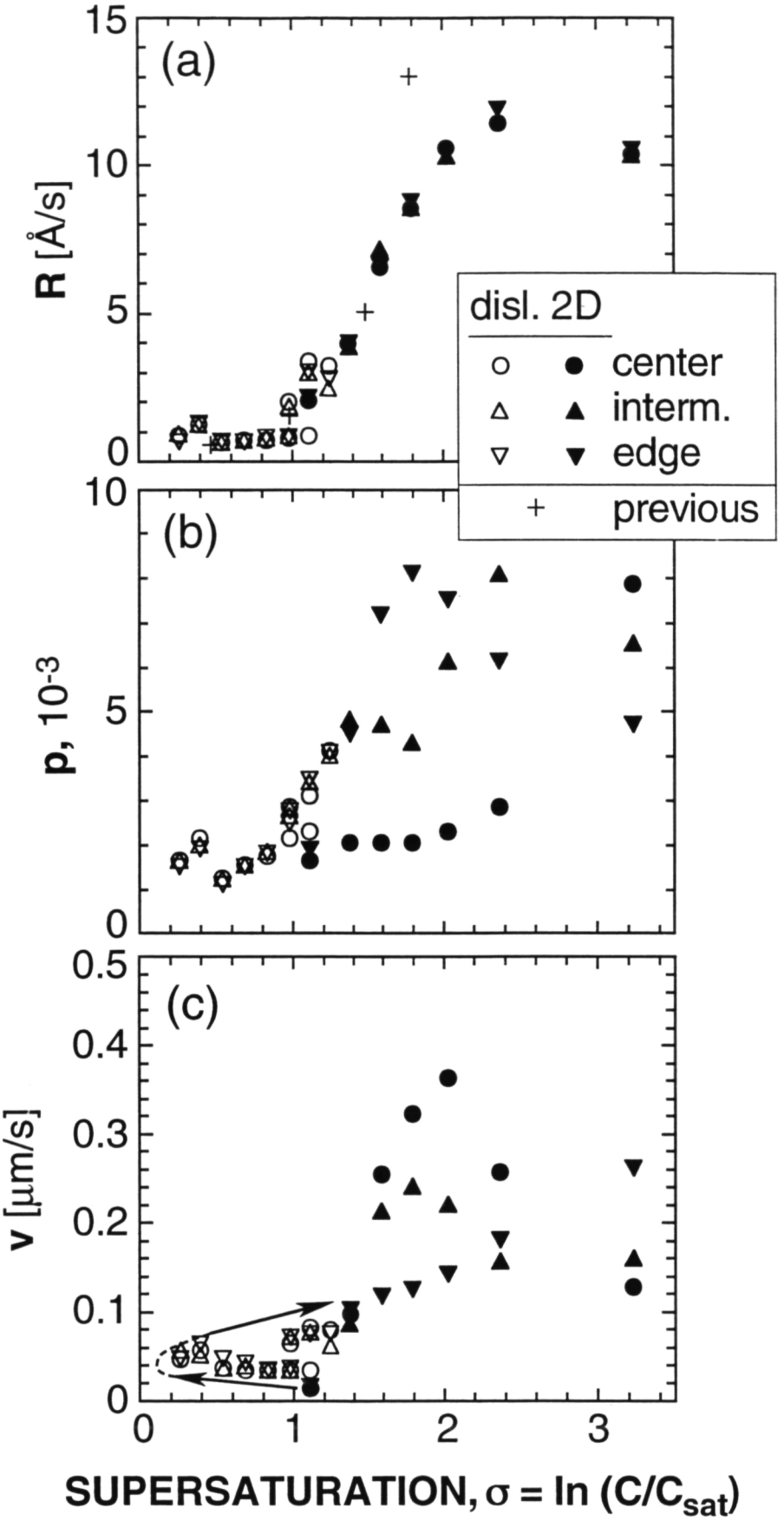
(a)
(b)
(c)
R [Å/s]
p, 10-3
v [μm/s]
disl. 2D
center
interm.
edge
previous
SUPERSATURATION, σ = ln (C/Csat)

FIG. 6

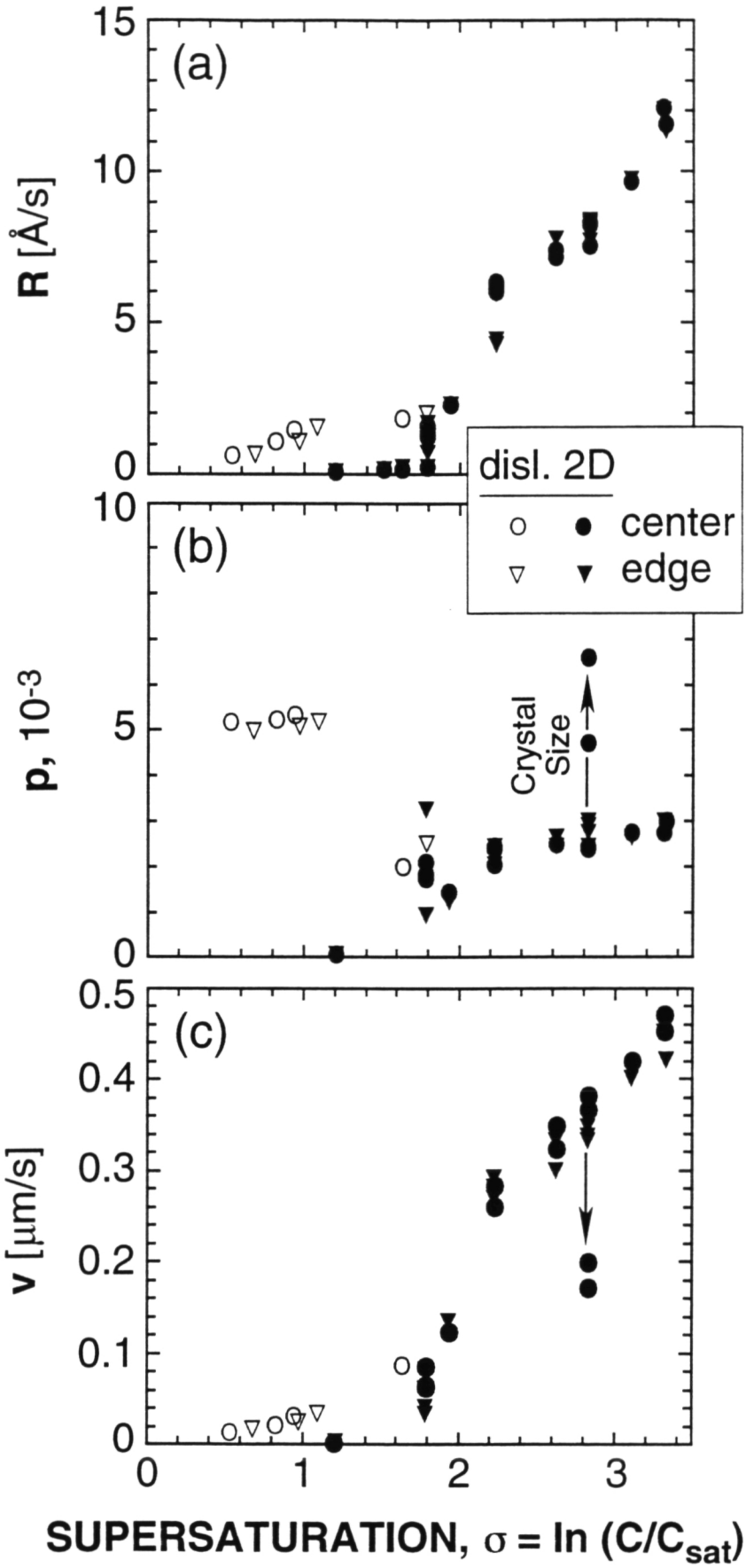
(a)
(b)
(c)
R [Å/s]
p, 10-3
v [μm/s]
disl. 2D
center
edge
Crystal Size
SUPERSATURATION, σ = ln (C/Csat)

FIG. 7

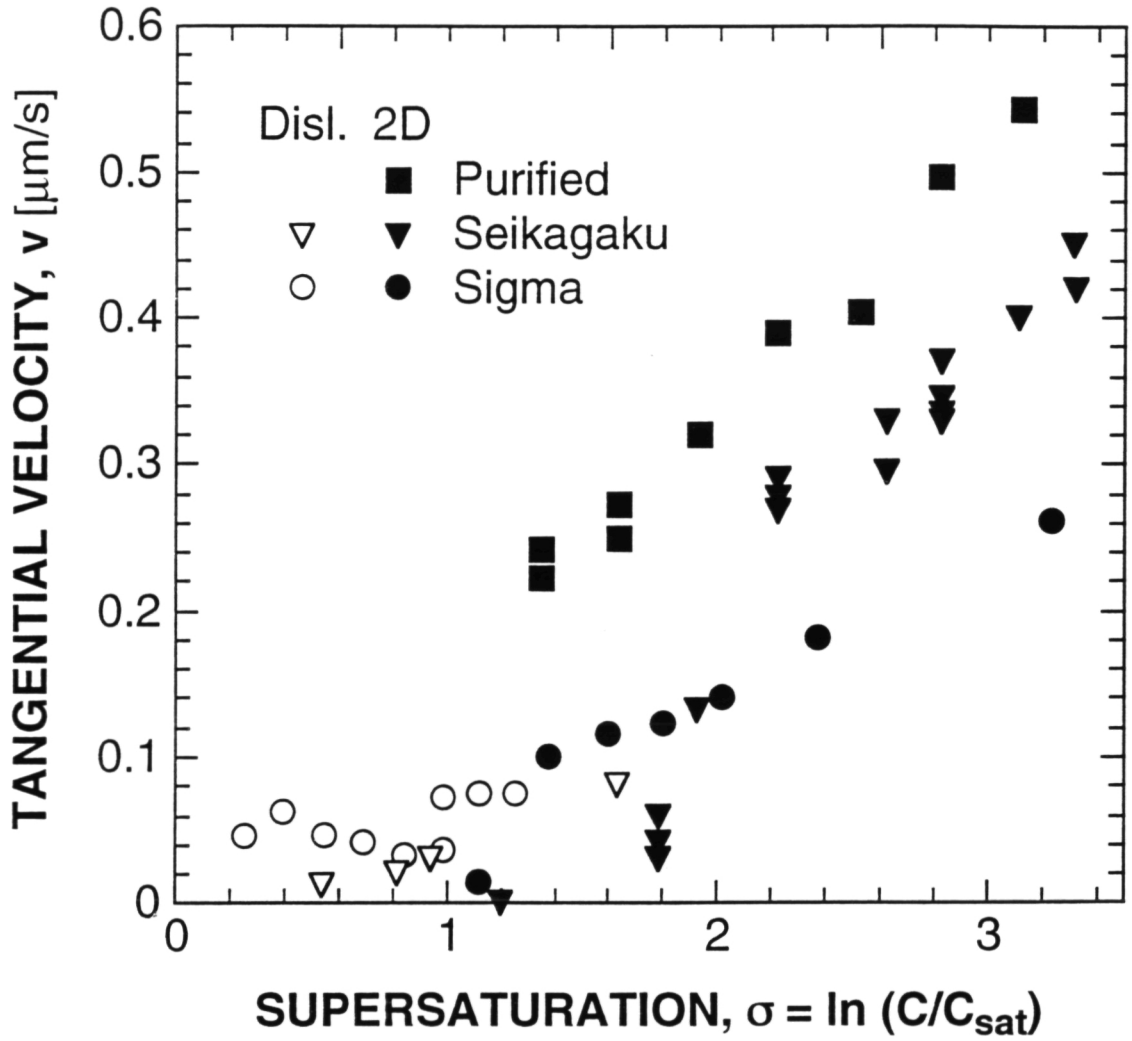
Disl. 2D
Purified
Seikagaku
Sigma
TANGENTIAL VELOCITY, v [μm/s]
SUPERSATURATION, σ = ln (C/C_sat)
0.6
0.5
0.4
0.3
0.2
0.1
0
0
1
2
3

FIG. 8

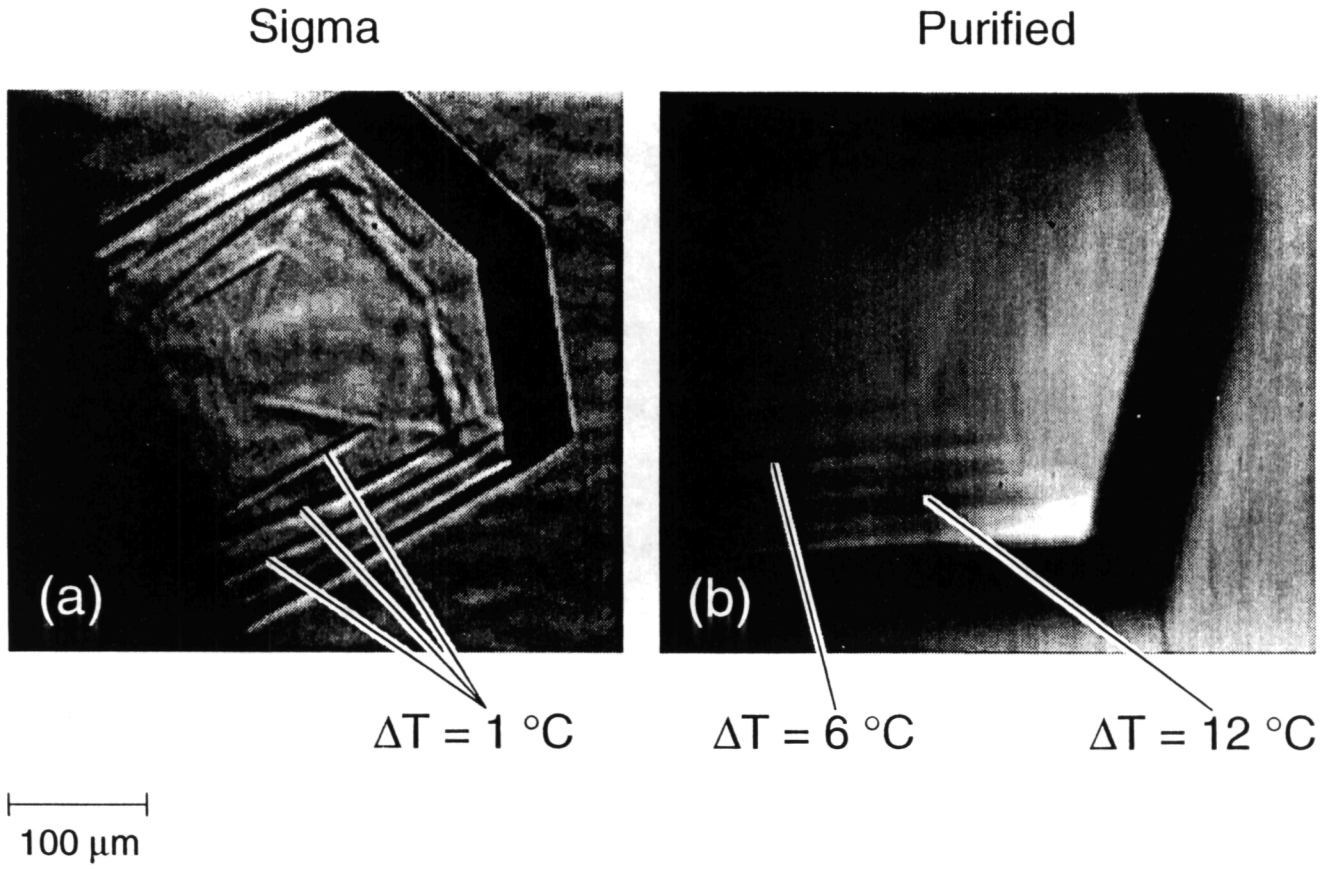

FIG. 9

CMMR MS 95-4 Accepted JCG August 1995

Facet morphology response to nonuniformities in nutrient and impurity supply. II. Numerical simulations

Hong Lin, Peter G. Vekilov and Franz Rosenberger

Center for Microgravity and Materials Research

University of Alabama in Huntsville, Huntsville, AL 35899, USA

Abstract

A model for the evolution of facet morphologies in growth from solutions is presented. The numerical model links, for the first time, bulk transport of solute and impurities in a solution growth cell with microscopic interfacial kinetics processes. The macroscopic transport is dealt with as in the 2D model [H. Lin et al., J. Crystal Growth 151 (1995) 153] of a crystallization cell used for lysozyme in our laboratory. The microscopic kinetics is incorporated through a meso-scale continuum model of growth step motion in response to the interfacial concentration distributions. Local growth step velocities are linearly interpolated from the values obtained at the grid points of the bulk transport simulation. Experimentally determined kinetics and transport coefficients are employed. We find that the facets remain *macroscopically* flat, in spite of the lower nutrient and impurity concentrations in the facet center regions. This stabilization is achieved through the formation of a *microscopic* depression in the facet, with *nonuniform* vicinal slope (step density). If the step density in the facet center exceeds a certain value, no further stabilization results on further steepening, and the facet loses its macroscopic morphological stability. This loss of morphological stability depends sensitively on the value of the steps' kinetic coefficient. For pure lysozyme-precipitant solutions, we obtain microscopic depressions with a higher slope at the facet center than at the edge. However, with an impurity that impedes step kinetics and is preferentially incorporated into the crystal, the simulations produce microscopic facet depressions with higher slope at the edge. Impurity depletion at the interface, due to low initial concentration and/or slow diffusion leads to mixed shapes, and eventually to shapes typical of growth from pure

solution. Quantitative agreement with facet morphologies observed on lysozyme crystals [P.G. Vekilov et al., JCG, accepted] is obtained, assuming overlap of the steps' diffusion fields.

1. Introduction

In a previous paper [1], we numerically simulated the growth of lysozyme crystals by coupling, on a macroscopic scale, transport in the bulk solution to isotropic interface kinetics through a simple proportionality between normal growth rate and local interfacial supersaturation. Both, convective-diffusive and purely diffusive transport simulations resulted in interfacial nutrient concentration nonuniformities of up to 20%. Within the realm of this limited kinetics model, these nonuniformities result in macroscopic depressions in the facet center; see also Sect. 3.1 below. In reality, however, a *macroscopically* planar growth shape is retained [2-4].

Our recent high-resolution measurements showed that this stabilization is achieved through the formation of a *microscopic* depression in the facet, with nonuniform vicinal slope (average step density) [5,6]. For pure lysozyme-precipitant solutions, we obtained depressions with a higher slope (step density) at the facet center than at the edge. This has been predicted theoretically [7-11] and illustrated in detail by Monte-Carlo simulations [12-14]. However, in the presence of an impurity that impedes step kinetics and is incorporated into the crystal, we observed, for the first time, microscopic facet depressions with a higher vicinal slope at the edge [6]. Motivated by these findings, we have now incorporated anisotropic interface kinetics into our earlier model. This is achieved by relating the local supersaturation to the step (tangential) velocity (rather than the normal growth rate R) and obtaining R as the product of the locally varying slope (step density) and step velocity. Based on experimentally determined transport and kinetics coefficients, this approach reproduces the observed vicinal morphologies.

2. Simulation model

The geometry and macroscopic transport aspects of the simulation model are identical to those used in our previous model for the isothermal solution growth of lysozyme [1]. In this work we found that convection causes only small changes in the distribution of the supersaturation

across the horizontal facet of the crystal considered here. Hence, to save computer time, convection was ignored in the morphology simulations presented here.

2.1. Coupling between bulk transport and step motion

The layer growth mechanism, which has been clearly established for tetragonal lysozyme [15-17], was incorporated as follows. As depicted in Fig. 1, growth step generation is assumed to take place at the facet edges only. This is typical for the high supersaturations assumed in the simulations [6,18]. From an assumed initial vicinal slope p^0, initially equidistant positions of the steps on the top facet are calculated as

$$x^0(n) = n(h/p^0) \,, \tag{1}$$

where $1 \leq n \leq N$ is the specific step number, and $h = 110$ Å is the unit cell dimension of lysozyme in the <110> direction [19,20]. Due to the symmetry of the system, only step positions on one half of crystal facet are calculated. Note that even for a p^0 as low as 10^{-3}, $N = 27$ for one half of the facet of the 600 μm wide crystal. Hence, the step positions represent a much finer scale than the 6 points on the macro-grid used across the half-width of the crystal for the bulk transport calculation in Ref. [1]. To somewhat improve the resolution in the macroscopic concentration distributions in the current model, we increased the number of grid points across the facet from 11 to 41.

The initial steps are assumed to move with tangential velocity $v(n)$. This is obtained by linear interpolation of the $v(X)$-values at the fixed macro-grid points X_i; see Fig. 1. The $v(X)$-values are calculated according to various kinetics laws $v[\sigma(X)]$; see below. As the steps move, their positions are periodically updated after time steps Δt used in the transport calculation according to

$$x^{(j+1)} = x^{(j)}(n) + v(n)\, \Delta t \,. \tag{2}$$

The Δt is chosen much shorter than macroscopic diffusion times. The supersaturations at the macro-grid points are updated with each time step.

New steps are generated at the edges with the rate v_e/d_e, where v_e and $d_e = h/p_e$ are the tangential velocity and the interstep distance at the facet edge, respectively, with p_e the local slope at the edge. For simplicity, we assume that p_e is proportional to the supersaturation at the edge σ_e. Thus, the interstep distance at the edge is calculated according to

$$d_e = d_e^0 \, (\sigma_e^0/\sigma_e) \, , \tag{3}$$

where d_e^0 and σ_e^0 are the initial interstep distance and supersaturation at the edge, respectively. When a new step is generated, that is as soon as $x(1) > d_e$, the old steps are renumbered by substituting $n+1$ for n. As soon as a step reaches the facet center ($x(N)$ = 300 μm), it is annihilated, and the total number of steps is decreased by 1. Since step generation and annihilation occur independently, N changes with the evolution of the vicinal shape. On "steeper" vicinal shapes, N can reach several hundred.

From the set of step positions $\{x(n)\}$ at a given time, the interstep distances

$$d(n) = x(n+1) - x(n), \tag{4}$$

and the local slopes

$$p(n) = h/d(n), \tag{5}$$

are calculated. The slopes at the macro-grid points $p(X)$ are then obtained by linear interpolation from neighboring $p(n)$-values. The normal growth rate is calculated from

$$R(X) = p(X) \, v[\sigma(X)] \, , \tag{6}$$

with the supersaturation defined as $\sigma = ln(\rho_1 / \rho_1^{eq})$, where ρ_1 is the transport-dependent interfacial lysozyme concentration and ρ_1^{eq} the equilibrium concentration of lysozyme at the growth conditions. The new $R(X)$-values are then used to update the boundary conditions (Eqs. 6 and 7 in Ref. [1]) for the transport calculations. Thus, Eq. (6) couples step kinetics and bulk transport. Note that in Ref. [1] the normal growth rate was denoted by Vf rather than R, and the

supersaturation was defined as a linear rather than logarithmic function of solute concentration. In the present work, we have studied only the evolution of the vicinal morphology of the top facet; see Ref. [1] for geometrical details. The normal growth rate on the two side faces of the crystal was assumed to be uniform and equal to the value at the edge of the top face.

2.2. *Kinetics models and coefficients*

2.2.1. Normal growth. As reference case for the effects of various step kinetics relations we have first, as in Ref. [1], ignored step motion and assumed that for this normal growth mode

$$R(X) = b_{face}\, \sigma(X). \tag{7}$$

The experimental value of the face kinetic coefficient $b_{face} = 8.5 \times 10^{-8}$ cm/s [6,18], is based on the above definition of supersaturation and, differs from the kinetic coefficient β used in Eq. (7) in Ref. [1]. For this and all following cases we set the initial supersaturation $\sigma^0 = 2.78$.

2.2.2. Step kinetics without step interaction. As a first approximation to the real system, we assumed that the local step velocity $v(X)$ is a function of the supersaturation $\sigma(X)$ only,

$$v(X) = b_{step}\, \sigma(X). \tag{8}$$

This applies to systems in which the characteristic surface diffusion length is much less than the interstep distance. In accordance with our findings with pure solutions [6], we set the step kinetic coefficient, $b_{step} = 1.7 \times 10^{-5}$ cm/s, and the initial slope at the facet edge $p_e^0 = 5 \times 10^{-3}$. Note that, with $b_{face} = b_{step}\, p_e^0$, the above values result in the same b_{face} as in Sect. 2.2.1, which allows for a quantitative comparison of the results obtained for these cases.

2.2.3. Step kinetics with step field overlap. In the companion paper [6], we provided evidence for the overlapping of both surface and bulk diffusion fields [21-23] in our system, rather than direct incorporation with bulk step field overlap only [21,24-26]. Then the dependence of tangential step velocity on the local supersaturation can be written as [6]

$$v(X) = \frac{b_{step}\sigma(X)}{1 + k\,p(X)}\,, \tag{9}$$

where $k\,p$ is a Peclet number characterizing the relative importance of serial bulk/surface diffusion and incorporation into steps from the surface, defined as $k = (\lambda^2/\Lambda_s h)(1 + \delta/\Lambda)$ [6]. The value of k was estimated as follows. For the characteristic surface diffusion length we assumed $\lambda = 1$ μm [6]. The characteristic distance for surface-step exchange, Λ_s, was set equal to λ [6]. Since Eq. (9) was obtained for the characteristic length for volume-surface incorporation (impedance of adsorption reaction) being large compared to λ, we assumed $\Lambda \geq 10\,\lambda$. As above, the step height $h = 110$ Å. In Ref. [1] we obtained for the width of the solute depletion zone (diffusion boundary layer width) $\delta \approx 150$ μm. However, in the reference experiments [6] the normal growth rates were considerably lower than in the earlier simulation [1]. Hence, the characteristic solutal convection velocities resulting from the lower interfacial concentration gradient were likely lower too, resulting in an increase in δ. Therefore, we set $\delta = 300$ μm. Under these assumptions we obtained $k \approx 3000$. The initial slope at the edge was again set to $p_e^0 = 5 \times 10^{-3}$ [6]. The step kinetic coefficient for this case was chosen as $b_{step} = 2.72 \times 10^{-4}$ cm/s. This value yields an effective step kinetic coefficient $b_{step}^{eff} = b_{step}/(1 + k\,p)$ similar to the previous case.

2.2.4. Impurity effects on step kinetics. For the case of step motion impediment by foreign adspecies, we assumed, as suggested by our experiments [6,18], that only impurities at steps affect step propagation. Since b_{step} is considered inversely proportional to the distance between free kinks along the step [27], we obtained [6]

$$v(X) = \frac{b_{step}\sigma(X)}{(1 + k\,p(X))(1 + \xi\,(\rho_2(X)/\rho_2^0))}\,. \tag{10}$$

Here, ρ_2^0 is the initial impurity concentration and ξ is a phenomenological coefficient for impurity action on step motion. Since we have observed that the presence of impurities does not strongly lower the tangential velocity, we assumed that $\xi = 2$. This value ensures, in agreement with experiments, that v is about half that obtained for the pure cases. The values of b_{step} and k were

the same as in the previous case. The slopes observed in growth from impure solutions were considerably higher than in the pure case [6]. Thus, we set $p_e^0 = 10^{-2}$.

For the bulk transport of the impurities additional assumptions were made. Since the gel electrophoresis results [6] showed that the protein impurities that are preferentially incorporated into lysozyme have a much higher molecular weight, the impurity diffusivity D_2 was set at half the value for lysozyme [1]. Furthermore, as estimated from the gel results, $\rho_2^0 = 2$ mg/ml, i.e. 25 times lower than the initial lysozyme concentration. To calculate the impurity incorporation rate into the crystal and, hence, the impurity flux towards the interface, we assumed an adsorption coefficient $\alpha = 100$. This adsorption coefficient is the ratio of impurity concentration in the adsorption layer to that in the bulk. For the volume of the adsorption layer we take the product of surface area and step height h. Since the change in lysozyme density with crystallization $(\rho_1^{cryst}/\rho_1^{sol}) > 16$, the above value of α ensures a considerably higher impurity to lysozyme ratio in the crystal than in the solution, as the gels in Ref. [6] indicate. Based on these parameters, we used the interfacial impurity boundary condition

$$-D_2 \nabla \rho_2 \cdot \boldsymbol{n} = \alpha \rho_2 R \,. \tag{11}$$

3. Results and discussion

3.1. Normal growth

Fig. 2a shows the normalized supersaturation $\sigma(X)/\sigma_e$ and growth rate $R(X)/R_e$ distributions across the facet after 5, 10 and 20 hours of crystal growth. The respective values at the facet edge, σ_e and R_e, used for normalization, are listed in Table 1 together with the initial values. Since proportionality between normal growth rate and supersaturation was assumed, see Eq. (7), their normalized distributions coincide. The surface shapes in Fig. 2b were obtained by integrating R over time, i.e.,

$$z(X) = \sum_{t=0}^{T} R(X,t)\,\Delta t \,. \tag{12}$$

One sees that, in contrast to the experimental observations [6], the facet depression increases with time in response to the increasingly nonuniform interfacial supersaturation.

3.2. *Step kinetics without step interaction*

The results for $\sigma(X)/\sigma_e$, $p(X)/p_e$ and $R(X)/R_e$ based on Eq. (8) are given in Fig. 3a. For the evolution of the σ_e-, p_e- and R_e-values see Table 1. The decrease in p_e results from the assumed proportionality between step generation rate and supersaturation at the edge of the facet. The decrease in supersaturation reflects the depletion of the nutrient. The interfacial supersaturation is higher at the facet edge than in the center, in agreement with experimental observations [28] and various modeling results [1,14,29-31]. Note that the nonuniformity in supersaturation remains essentially constant at about 2%, in contrast to the increase to almost 4% in the normal growth mode. The difference of R/R_e between the edge and center remains less than 0.3%. Hence, even the simplest linear assumption for $v(\sigma)$ results in uniform R over the facet.

As shown in Fig. 3b, the facet depression is less than 1.5 μm across 600 μm, i.e., the facet remains macroscopically flat. However, on a microscopic scale the interfacial shape is slightly convex. Of a pair of steps that moves down the supersaturation gradient, the trailing step is always exposed to higher supersaturations and, thus, moves faster than the leading step. As a consequence the step density increases towards the center of the facet. This result corroborates the prediction of stability theory of polyhedral crystal growth [7-9]. That is, the slope increases with distance from the facet edge to compensate for the transport-induced supersaturation inhomogeneity. Note that the slope ratio p_c/p_e is less than 1.03, in contrast to our experimental finding of about 2 [6]. As discussed in Ref. [6], this discrepancy is likely due to strong overlap of the step supply fields, that was unaccounted for in the above simulations.

3.3. *Step kinetics with step field overlap*

For this case, the step velocity was calculated from Eq. (9). The resulting distributions of $\sigma(X)/\sigma_e$, $p(X)/p_e$ and $R(X)/R_e$ are shown in Fig. 4a and 4b. The corresponding values of σ_e, p_e and R_e are again listed in Table 1. In spite of increased nonuniformity in supersaturation, the

nonuniformity in normal growth rates is further reduced to about 0.2%. Moreover, due to the strong step field overlap, the slope ratio p_c/p_e increases to 1.6. This is in good agreement with the observations in [6]. The corresponding interfacial shapes are shown in Fig. 4c. Note that, despite the increase of interfacial supersaturation nonuniformity with time, the facet depression decreases.

In order to investigate the effects of the facet step kinetic coefficient b_{step} on the morphology, we simulated a case with a doubled value ($b_{step} = 5.44 \times 10^{-4}$ cm/s) and otherwise same conditions. As illustrated by Fig. 5a, the initially doubled normal growth rate results in a stronger nonuniformity of the interfacial supersaturation. Note the increase of p_c/p_e to 12 in Fig. 5b. This nonuniformity in vicinal slope is about six times larger than the experimentally observed one [6]. The corresponding strongly convex facet shapes are shown in Fig. 5c. The continuous deepening of the facet depression indicates that further increases in the slope in the center region can no longer compensate for the σ-nonuniformity. When the steps already compete for nutrient, the nutrient utilization cannot be further increased by further increases in step density. As a consequence, the nonuniformity in R/R_e increases with time and, eventually, morphological stability is lost. The two cases dealt with in this section well illustrate the sensitive response of the microscopic interface shape to changes in the step kinetic coefficient.

3.4. Impurity effects on step kinetics

Fig. 6a presents the evolution of the nonuniform interfacial impurity distribution obtained for this case. One sees that the preferential impurity incorporation into the crystal causes lower ρ_2-values at the facet center than at the edge. This is due to the more ready replenishment of the impurity to the edges. As the crystal grows, the impurity in the solution is continuously depleted. This is illustrated by the consecutive horizontal concentration profiles, taken at the crystal half-height, depicted in Fig. 7a. Figs. 6b-d present the results for $\sigma(X)/\sigma_e$, $p(X)/p_e$, $R(X)/R_e$ and $z(X)$ for this case. Since our assumptions for the impurity effect cause a reduction in growth rate, the curves were chosen for 10, 20 and 40 hours of crystal growth.

From Fig. 6c we can deduce that initially the growth steps are more retarded at the periphery of the facet than in its center. Hence, we obtain p/p_e-values lower than unity. After

about 7 hours of growth (not shown in the figure), the slope at the edge was about 2.5 times that at the facet center. This magnitude is in fair agreement with the experimental results (see Fig. 5, 6, 7 in Ref. [6]). Correspondingly, as depicted in Fig. 6d, a microscopically *concave* interface is obtained, in contrast to the *convex* vicinal shapes of growth from pure solutions. Note that during this initial phase the nonuniformity in impurity distribution (Fig. 6a) is much more pronounced than that in the lysozyme supersaturation. This is the result of the lower diffusivity and preferential incorporation of the impurity.

As growth proceeds, with continuous depletion of the impurity, its impeding effect on kinetics is reduced. Hence, the growth rate increases (see Table 1) and the nonuniformity in lysozyme supersaturation becomes comparable to that of the impurity concentration. This results in a transition of the growth morphology from the impurity-conditioned, concave shape to the solute-conditioned, convex shape after about 20 hours. Such a transition was also observed in our morphological studies of growth from impure solutions (see Figs. 7c and d in Ref. [6]).

4. Summary and Conclusions

We have numerically simulated the development of interface morphologies and kinetics during the growth of tetragonal lysozyme crystals. For the first time, our model links bulk transport of solute and impurities in a solution growth cell with microscopic interfacial kinetics processes. This description of the dependence of step generation and propagation on the transport-conditioned solution composition at the interface yields microscopic interface profiles that are in good agreement with experimental observations.

We found that, irrespective of the specific formulation, anisotropic interface kinetics tend to result in uniform normal growth rates over the crystal facet and, thus act morphologically stabilizing on a macroscopic scale. This is in agreement with general observations of macroscopically flat growth facets in the presence of nonuniform solute supply.

On a microscopic scale, in growth from pure solutions, the vicinal slope at the facet center is higher than at the edge. This convex shape compensates for the lower supersaturation and, hence, lower step velocity in the center region. If no step interaction is assumed, the slope ratio

between the center and the periphery is inverse proportional to the ratio of the local supersaturations. For the crystal size considered, this ratio remains below 1.02. However, if step-field overlap is assumed, using a Peclet number compatible with the experimental observations, the slope at the facet center can be up-to 2 times as high as at the edge. This is in good agreement with experimental values. If the step density (vicinal slope) in the facet center exceeds a certain value, no further stabilization results on further steepening, and the facet loses its macroscopic morphological stability. This loss of stability depends sensitively on the value of the steps' kinetic coefficient. Similarly, the initial vicinal slopes used in the simulations must be realistic. Excessive assumed slopes cause nonuniformities in supersaturation and growth rate that overpower the stabilizing effect of kinetics.

If step motion-impeding impurities are incorporated into the crystal, their lower concentration at the facet center results in faster step velocities and, thus, lower slope in this region. This concave shape also stabilize the facet morphology. If the impurity diffusivity is lower than that of the solute, during growth the interfacial impurity concentration decreases more rapidly than the interfacial supersaturation. This can cause a transition from the impurity-conditioned concave to the solute-conditioned convex vicinal interface shape.

Acknowledgments

This work has been supported by the Microgravity Science and Applications Division of the National Aeronautics and Space Administration (Grant # NAG8-950), and the State of Alabama through the Center for Microgravity and Materials Research at the University of Alabama in Huntsville. We also thank Lynne Carver for preparing the illustrations.

References

[1] H. Lin, F. Rosenberger, J.I.D. Alexander and A. Nadarajah, J. Crystal Growth 151 (1995) 153.

[2] L.A. Monaco and F. Rosenberger, J. Crystal Growth 129 (1993) 465.

[3] P.G. Vekilov, M. Ataka and T. Katsura, J. Crystal Growth 130 (193) 317.

[4] P.G. Vekilov, Progr. Crystal Growth Charact. 26 (1993) 25.

[5] P.G. Vekilov, L.A. Monaco and F. Rosenberger, J. Crystal Growth 148 (1995) 289.

[6] P.G. Vekilov, L.A. Monaco and F. Rosenberger, J. Crystal Growth, accepted.

[7] A.A. Chernov, J. Crystal Growth 24/25(1974) 11.

[8] T. Kuroda, T. Irisawa and A. Ookawa, J. Crystal Growth 42 (1977) 41.

[9] C. Kumar and J. Estrin, J. Crystal Growth 51 (1981) 323.

[10] A.M. Ovrutskii, Soviet Phys.-Cryst. 24 (1979) 327.

[11] A.A. Chernov and T. Nishinaga, in: Morphology of Crystals, Ed. I Sunagawa (Terra, Tokyo, 1987) Ch. 3, p. 207.

[12] R.F. Xiao, J.I.D. Alexander and F. Rosenberger, Physical Review A, 38(5) (1988) 2447.

[13] R.F. Xiao, J.I.D. Alexander and F. Rosenberger, J. Crystal Growth 100 (1990) 313.

[14] R.F. Xiao, J.I.D. Alexander and F. Rosenberger, Physical Review A, 43(6) (1991) 2977.

[15] S.D. Durbin and G. Feher, J. Mol. Biol. 212 (1990) 763.

[16] S.D. Durbin and W.E. Carlson, J. Crystal Growth 122 (1992) 71.

[17] S.D. Durbin, W.E. Carlson and M.T. Saros, J. Phys. D: Appl. Phys. 26 (1993) B 128.

[18] P.G. Vekilov and F. Rosenberger, J. Crystal Growth (accepted).

[19] L.K. Steinrauf, Acta Cryst. 12 (1959) 77.

[20] C.C.F. Blake, G.A. Mair, A.C.T. North, D.C. Phillips and V.R. Sarma, Proc. Roy. Soc. London B 167 (1967) 365.

[21] W.K. Burton, N. Cabrera and F.C. Frank, Phil. Trans. Roy. Soc. London A243 (1951) 299.

[22] G.H. Gilmer, R. Ghez and N. Cabrera, J. Crystal Growth 8 (1971) 79.

[23] J.P. van der Eerden, J. Crystal Growth 56 (1982) 174.

[24] A.A. Chernov, Soviet Phys. - Uspekhi 4 (1961) 116.

[25] A.A. Chernov, Contemp. Phys. 30 (1989) 251.

[26] A.A. Chernov, Crystal Growth Charact. 26 (1993) 121.

[27] A.A. Chernov, Modern Crystallography III, Growth of Crystals (Springer, Berlin, 1984) p. 161.

[28] S.P.F. Humphreys-Owen, Proc. Roy. Soc. A, 197 (1949) 218.

[29] A. Seeger, Phil. Mag. 44 (1953) 348.

[30] W.R. Wilcox, J. Crystal Growth 37 (1977) 229.

[31] W.R. Wilcox, J. Crystal Growth 38 (1977) 73.

Table 1. Compilation of simulation results.

Case	Time [h]	σ_e	p_e	R_e [Å/s]
Fig. 2	0	2.78	—	23.63
	5	2.37	—	20.15
	10	2.15	—	18.29
	20	1.69	—	14.41
Fig. 3	0	2.78	5×10^{-3}	23.64
	5	2.42	4.35×10^{-3}	17.90
	10	2.26	4.07×10^{-3}	15.64
	20	1.98	3.56×10^{-3}	11.96
Fig. 4	0	2.78	5×10^{-3}	23.64
	5	2.38	4.28×10^{-3}	20.0
	10	2.17	3.91×10^{-3}	18.12
	20	1.75	3.16×10^{-3}	14.35
Fig. 5	0	2.78	5×10^{-3}	47.27
	5	1.96	3.53×10^{-3}	32.45
	10	1.57	2.86×10^{-3}	25.50
	20	0.95	1.74×10^{-3}	14.48
Fig. 6	0	2.78	1.0×10^{-2}	8.13
	10	2.39	8.61×10^{-3}	14.27
	20	2.05	7.36×10^{-3}	13.63
	40	1.22	4.4×10^{-3}	8.69

Figure captions

Fig. 1. Model for step motion in nonuniform supersaturation at faceted interface. Upper part: meso-scale view of vicinal interface; continuum coordinate x for step position. Lower part: macroscopic view of interface with supersaturation distribution and discrete grid points (X_i) used in macroscopic transport simulation.

Fig. 2. Effects of normal growth from pure solution. (a) Distributions of normalized supersaturation and normal growth rate across the facet. (b) Facet shapes after 5, 10 and 20 hours of growth, dashed line: initial shape.

Fig. 3. Effects of step kinetics without step field overlap in growth from pure solutions. (a) $\sigma(X)/\sigma_e$, $p(X)/p_e$ and $R(X)/R_e$. (b) $z(X)$ after 5, 10 and 20 hours of growth, dashed line: initial shape.

Fig. 4. Effects of step field overlap in growth from pure solutions. (a) $\sigma(X)/\sigma_e$, and $R(X)/R_e$. (b) $p(X)/p_e$. (c) $z(X)$ after 5, 10 and 20 hours of growth, dashed line: initial shape.

Fig. 5. Effects of increased the step kinetic coefficient. (a) $\sigma(X)/\sigma_e$ and $R(X)/R_e$. (b) $p(X)/p_e$. (c) $z(X)$ after 5, 10 and 20 hours of growth, dashed line: initial shape.

Fig. 6. Effects of impurity-impeded kinetics. (a) $\rho_2(X)/\rho_{2e}$. (b) $\sigma(X)/\sigma_e$ and $R(X)/R_e$, (c) $p(X)/p_e$. (d) $z(X)$ after 10, 20 and 40 hours of growth, dashed line: initial shape.

Fig. 7. Concentration profiles in the solution at crystal half height: (a) impurity, (b) protein.

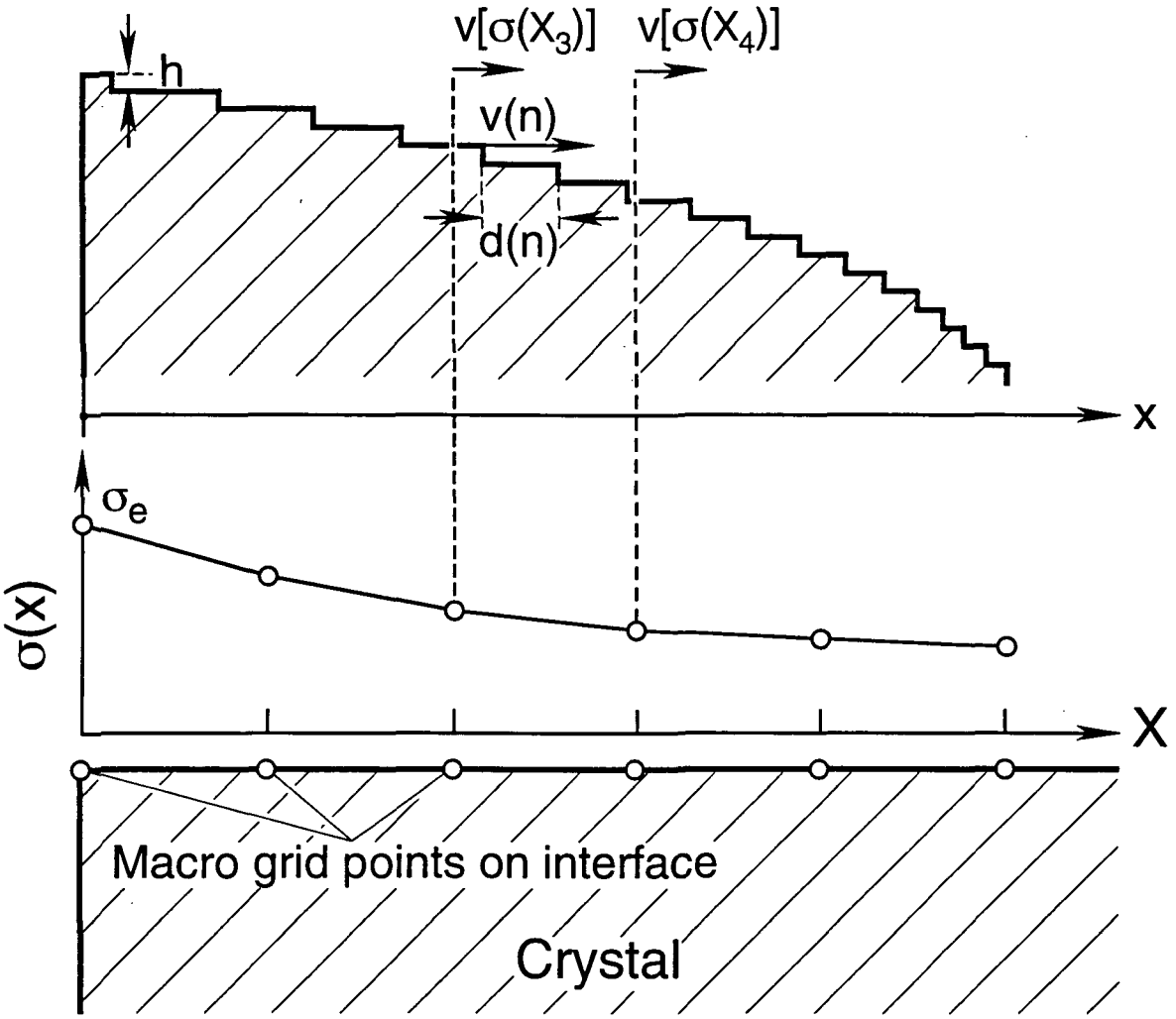
v[σ(X3)]
v[σ(X4)]
h
v(n)
d(n)
x
σe
σ(x)
X
Macro grid points on interface
Crystal

FIG. 1

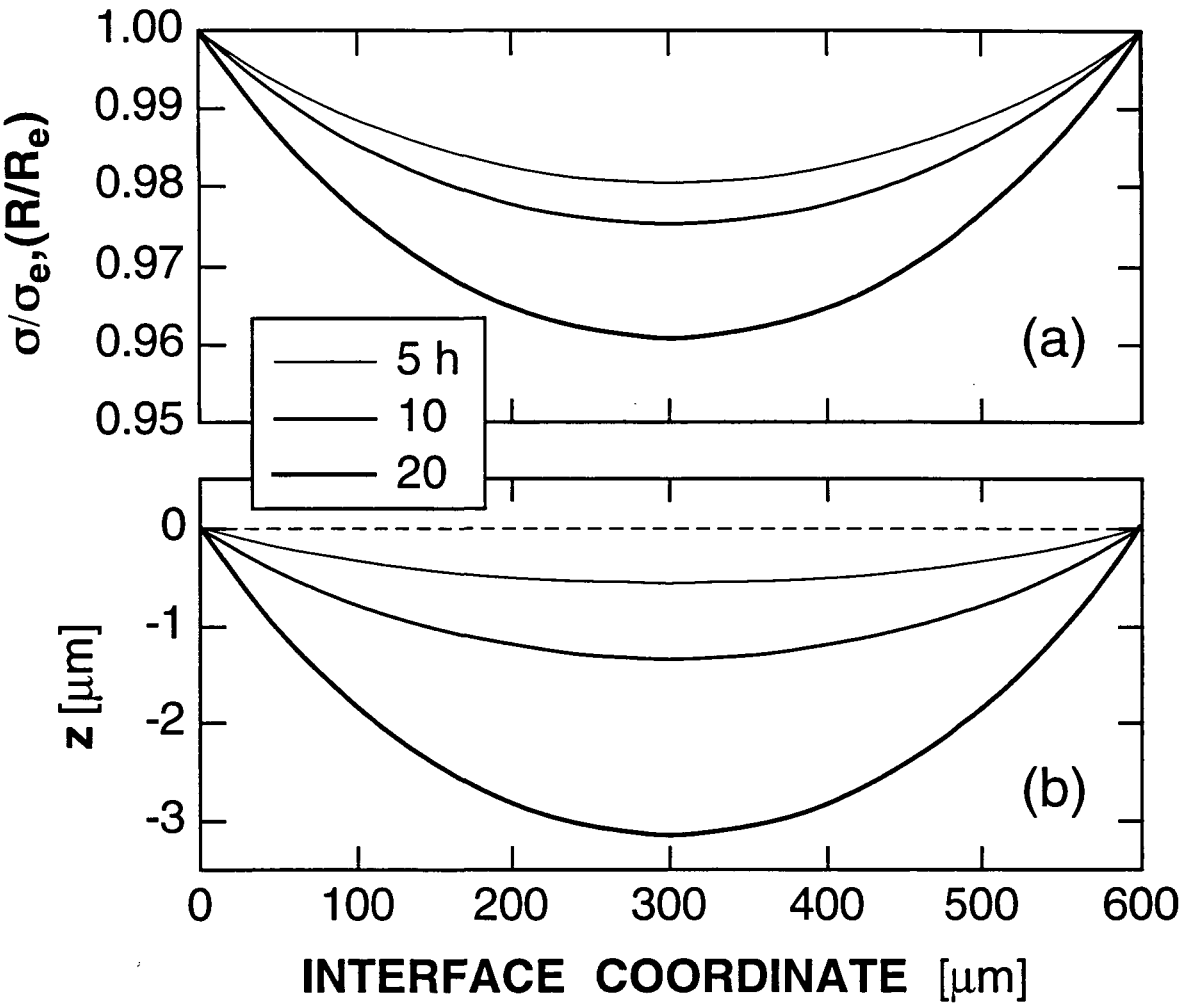
1.00
0.99
0.98
0.97
0.96
0.95
σ/σe,(R/Re)
5 h
10
20
(a)
0
-1
-2
-3
z [μm]
(b)
0
100
200
300
400
500
600
INTERFACE COORDINATE [μm]

FIG. 2

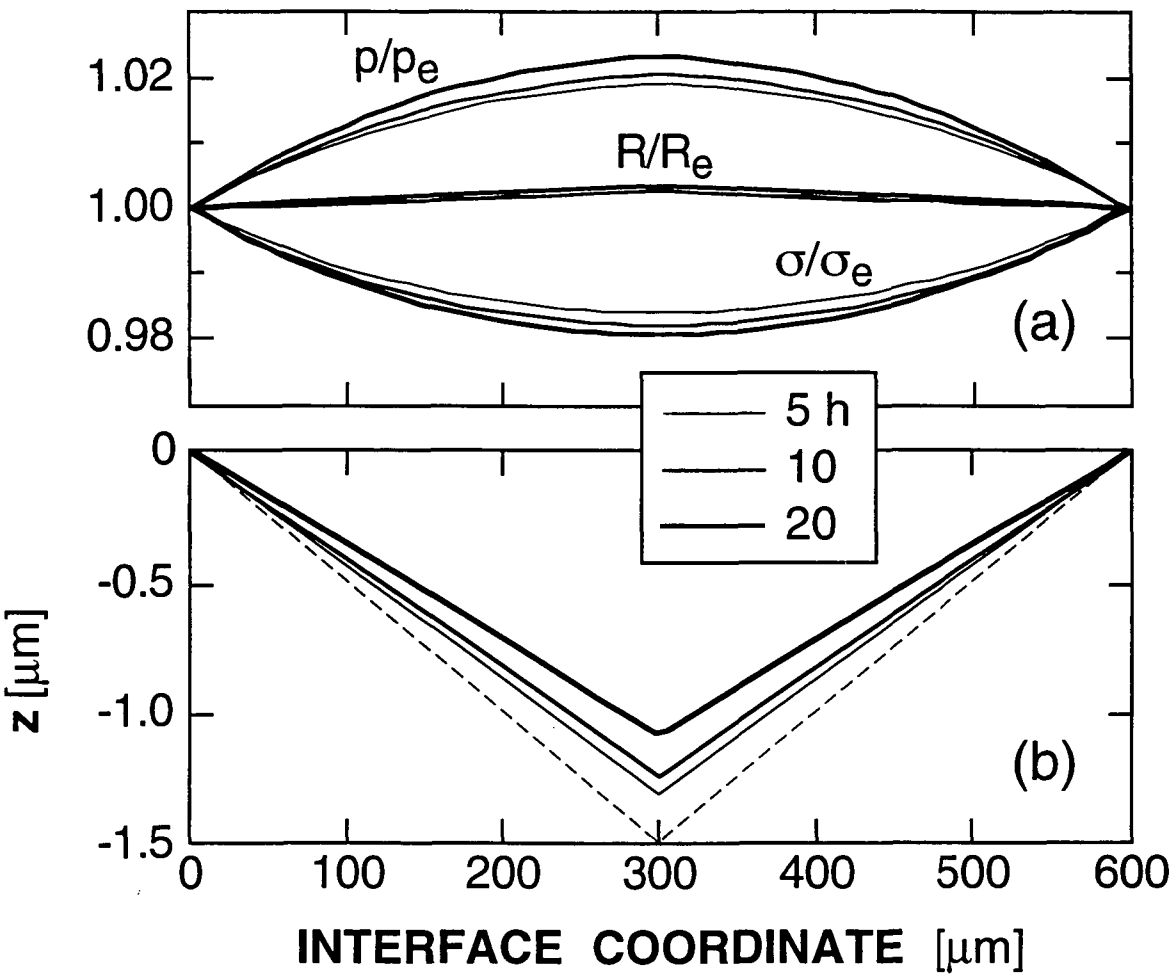
1.02
1.00
0.98
p/pe
R/Re
σ/σe
(a)
5 h
10
20
0
-0.5
-1.0
-1.5
z [μm]
(b)
0
100
200
300
400
500
600
INTERFACE COORDINATE [μm]

FIG. 3

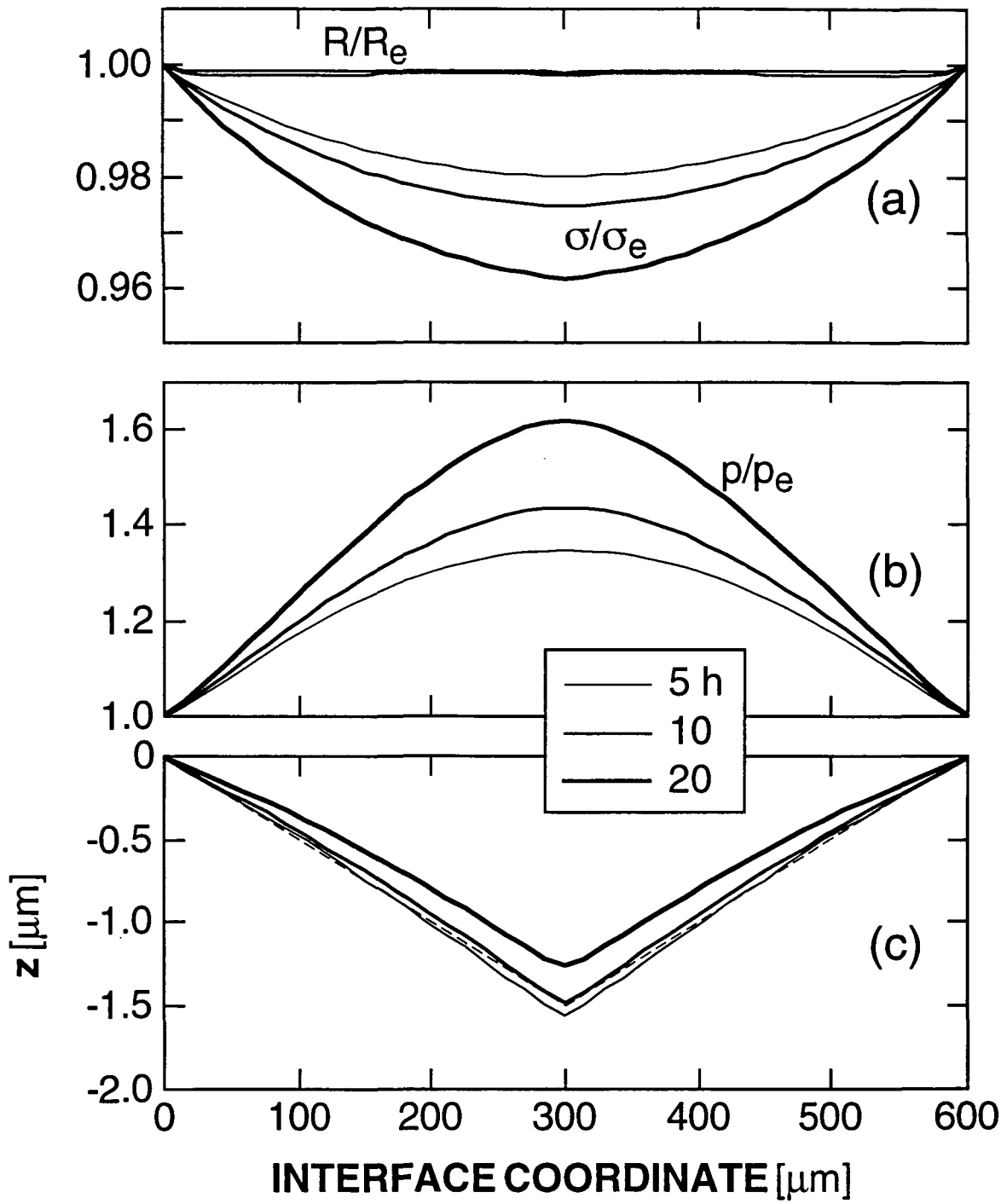
R/Re
1.00
0.98
0.96
σ/σe
(a)
1.6
1.4
1.2
1.0
p/pe
(b)
5 h
10
20
0
-0.5
-1.0
-1.5
-2.0
z [μm]
(c)
0
100
200
300
400
500
600
INTERFACE COORDINATE [μm]

FIG. 4

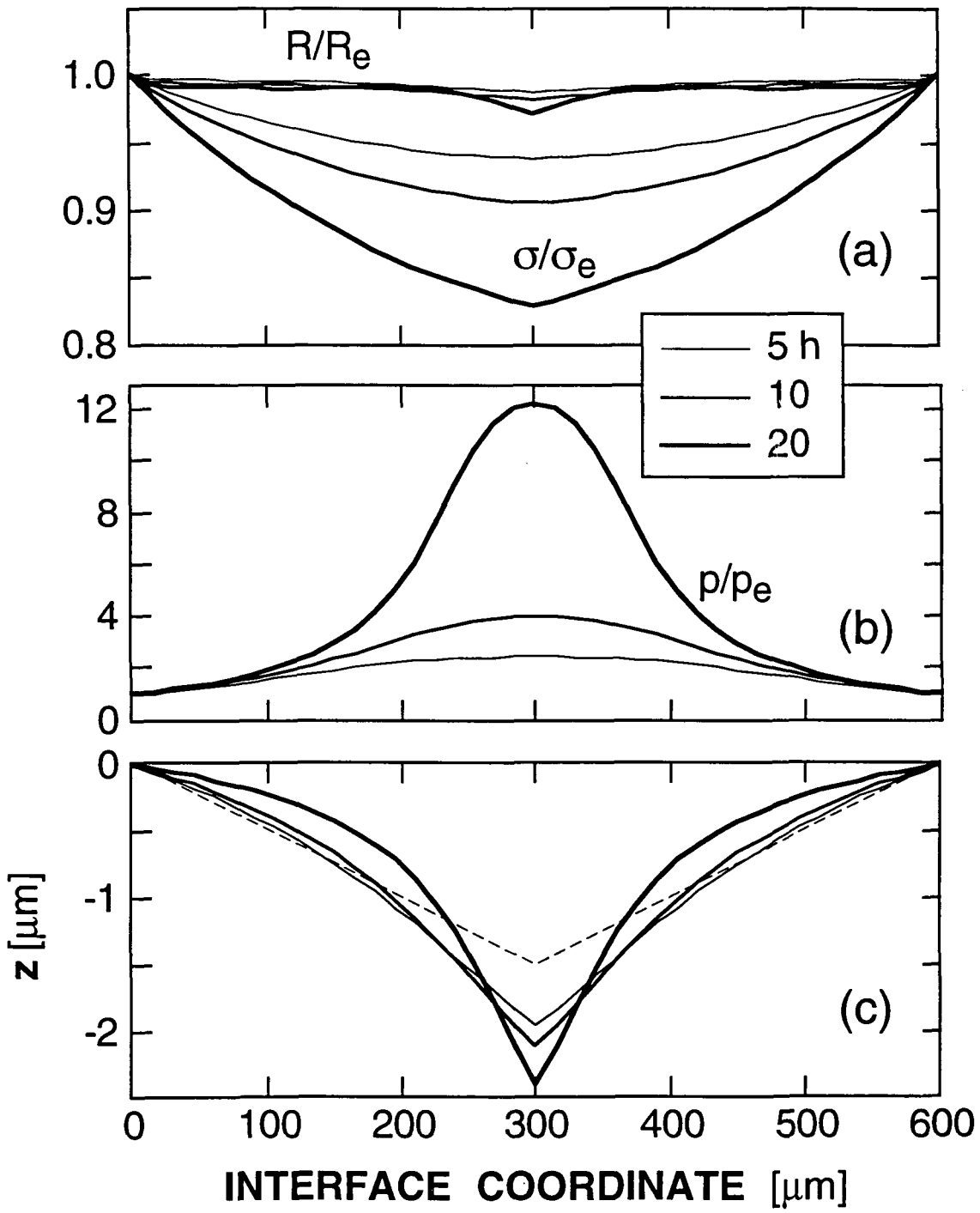
R/Re
1.0
0.9
0.8
σ/σe
(a)
5 h
10
20
12
8
4
0
p/pe
(b)
0
-1
-2
z [μm]
(c)
0
100
200
300
400
500
600
INTERFACE COORDINATE [μm]

FIG. 5

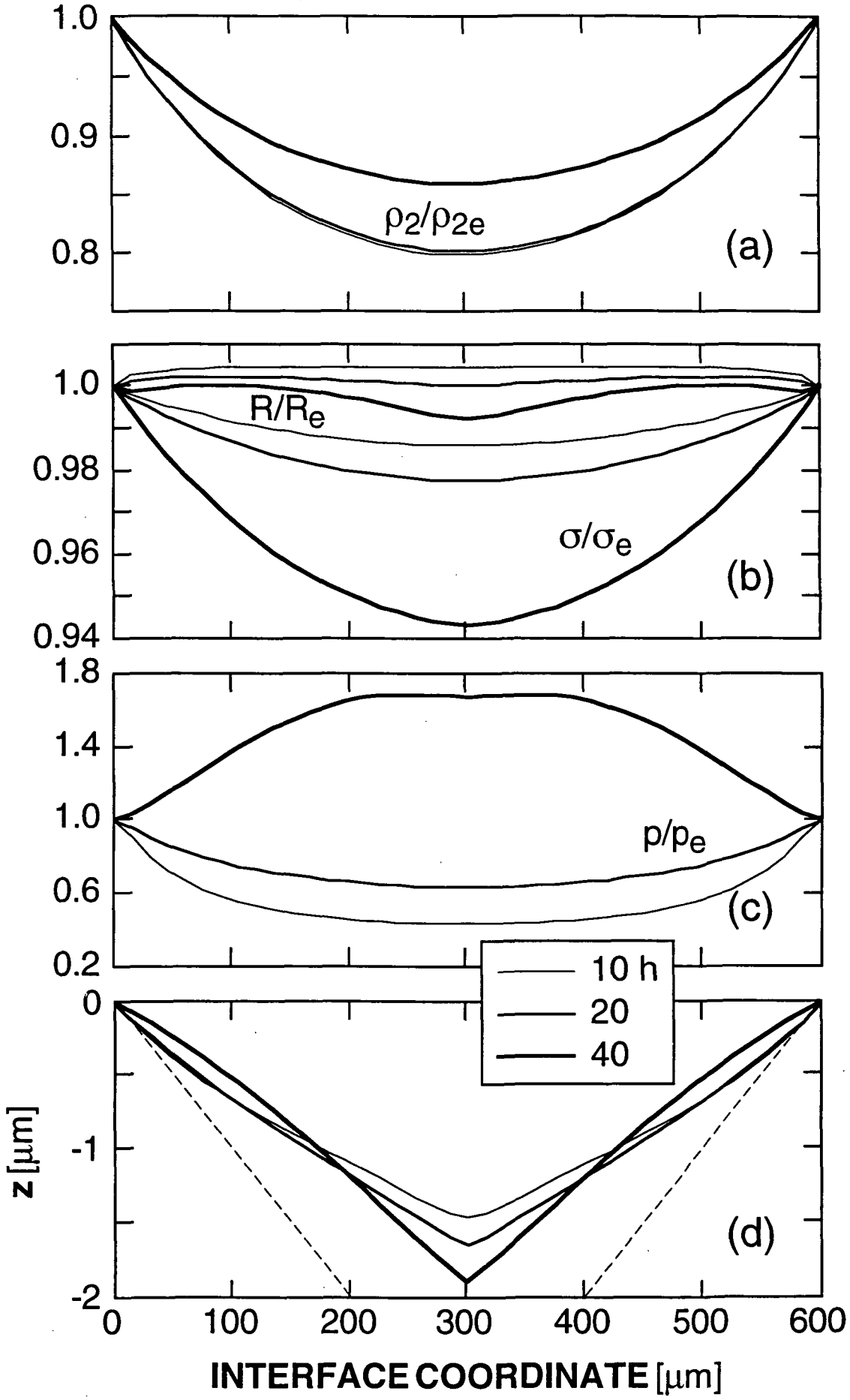
1.0
0.9
0.8
ρ2/ρ2e
(a)
1.0
0.98
0.96
0.94
R/Re
σ/σe
(b)
1.8
1.4
1.0
0.6
0.2
p/pe
(c)
10 h
20
40
0
-1
-2
z [μm]
(d)
0
100
200
300
400
500
600
INTERFACE COORDINATE [μm]

FIG. 6

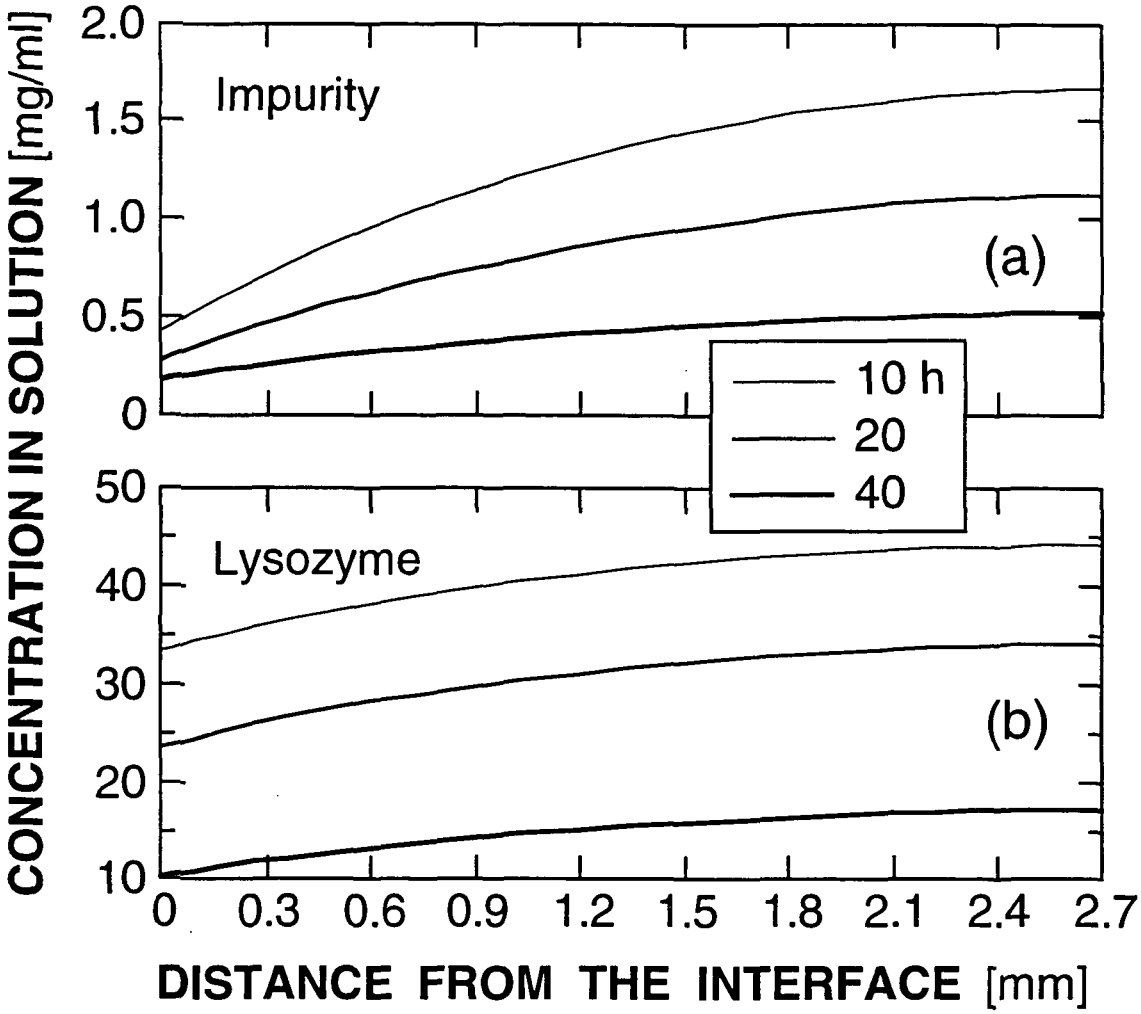
CONCENTRATION IN SOLUTION [mg/ml]
2.0
1.5
1.0
0.5
0
Impurity
(a)
10 h
20
40
50
40
30
20
10
Lysozyme
(b)
0
0.3
0.6
0.9
1.2
1.5
1.8
2.1
2.4
2.7
DISTANCE FROM THE INTERFACE [mm]

FIG. 7

Interactions in under- and supersaturated lysozyme solutions. Static and dynamic light scattering results.

Martin Muschol and Franz Rosenberger

Center for Microgravity and Materials Research

University of Alabama in Huntsville, Huntsville AL 35899, USA

We have performed multi-angle static and dynamic light scattering studies of lysozyme solutions at pH = 4.7. The Rayleigh ratio R_θ and the collective diffusion coefficient D_c were determined as function of both protein concentration c_p and salt concentration c_s with two different salts. At low salt concentrations, the scattering ratio Kc_p/R_θ and diffusivity increased with protein concentration above the values for a monomeric, ideal solution. With increasing salt concentration this trend was eventually reversed. The hydrodynamic interactions of lysozyme in solution, extracted from the combination of static and dynamic scattering data, decreased significantly with increasing salt concentration. These observations reflect changes in protein interactions, in response to increased salt screening, from net repulsion to net attraction. Both salts had the same qualitative effect, but the quantitative behavior did not scale with the ionic strength of the solution. This indicates the presence of salt specific effects. At low protein concentrations, the slopes of Kc_p/R_θ and D_c *vs.* c_p were obtained. The dependence of the slopes on ionic strength was modeled using a DLVO potential for colloidal interactions of two spheres, with the net protein charge Ze and Hamaker constant A_H as fitting parameters. The model reproduces the observed variations with ionic strength quite well. Independent fits to the static and dynamic data, however, led to different values of the fitting parameters. These and other shortcomings suggest that colloidal interaction models alone are insufficient to explain protein interactions in solutions.

I. INTRODUCTION

The difficulty of growing protein crystals has become an impediment to molecular structure determinations. The crystallization conditions depend on a large number of parameters. These include the solution temperature and pH, precipitant type and concentration, protein concentration and purity. The incremental variation of all these parameters in screening for crystallization conditions is very time consuming. In addition, many proteins are only available in μg quantities. Therefore it is important to establish correlations between readily measurable solution properties and crystallization conditions. Both static and dynamic light scattering have been applied in studies of protein solutions for decades, primarily to obtain molecular weights [1] and diffusivities [2]. In protein crystallization studies, light scattering was used to determine nucleation conditions and associated solution parameters [3-13].

Recently, George and Wilson [4] employed static light scattering to determine the sign and magnitude of the second virial coefficient to characterize the net interactions of proteins in undersaturated solutions. They found that reported crystallization conditions for numerous globular proteins in various precipitants correlate with a band of slightly negative virial coefficients. These results motivated us to study protein interactions in under- and supersaturated lysozyme solutions with simultaneous static and dynamic light scattering. In particular, we explored the changes in diffusivities and scattering intensities with protein concentration at several fixed salt concentrations employing two different salts. Furthermore, we tested the applicability of a colloidal interaction model to lysozyme. We modeled the dependence of the scattering intensity and diffusivity on ionic strength employing a DLVO potential for colloidal interactions. Values for the net protein charge Ze and Hamaker constant A_H were obtained for different approximations to the electrostatic repulsion term.

In the following, we first introduce the theoretical framework for the presentation of our light scattering data in Sect. II. The sample preparation and experimental techniques are described in Sect. III. Sect. IV contains the results. The data are discussed in terms of a colloidal interaction model in Sect. V. A summarizing discussion of our findings is given in Sect. VI.

II. THEORETICAL CONSIDERATIONS

Macromolecules in solutions scatter light due to the thermally induced fluctuations in local concentration. To relate the scattering caused by the protein to its properties, the excess scattering intensity per unit volume and solid angle is normalized by the incident intensity. This Rayleigh ratio R_θ can be expressed as [14]

$$R_\theta = KMc_p P(q)S(q) \ . \tag{1}$$

Here, K is the system-specific constant

$$K = \frac{4\pi^2 n_0^2}{N_A \lambda^4}\left(\frac{dn}{dc_p}\right)^2, \tag{2}$$

with n_0 the solvent's refractive index, N_A Avogadro's number, λ the wavelength, (dn/dc_p) the refractive index increment of the protein, where c_p is the protein's mass density. M is the molecular weight of the protein (solute). $P(q)$ and $S(q)$ are the form- and static structure-factor, which account for intraparticle and interparticle interference effects, respectively. The length scale over which light scattering probes the solution is set by the scattering wave number

$$q = \frac{4\pi n}{\lambda}\sin\left(\frac{\theta}{2}\right), \tag{3}$$

where θ is the scattering angle. With its radius $a \approx 20$ Å [15], and thus, $a << q^{-1}$, lysozyme is a Rayleigh scatterer, for which $P(q) = 1$. The mean experimental protein spacing $d = n_p^{-1/3}$, where n_p is the protein number concentration, equals 7.2 nm at the lowest concentration. Since this is considerably shorter than our range for the inverse wave number, 36 nm $< q^{-1} <$ 120 nm, our solution conditions fall within the long wavelength limit $d << q^{-1}$. In this limit the static structure factor $S(q=0)$ can be described by a virial expansion in the solute concentration . To first order in c_p , Eq. (1) becomes [16]

$$\frac{Kc_p}{R_\theta} = \frac{1}{M} + B_2 c_p. \tag{4}$$

B_2 is the second virial coefficient, which is positive for net repulsion, negative for net attraction and vanishes for ideal, "noninteracting" particles. Thus, for fixed solute concentration, Eq. (4)

indicates that net attractive/repulsive interactions enhance/reduce the light scattering intensity above/below the value KMc_p characteristic of an ideal system. Given that $P(q) = 1$, a comparison of Eqs. (1) and (4) identifies the static structure factor $S(q=0)$ as the ratio of the measured scattering intensity to its ideal solution value.

Dynamic light scattering (DLS) measurements utilize the temporal correlations of the scattering intensity fluctuations, which are related to the Brownian motion of the solute. For the general theory and typical applications of DLS see Refs. [2, 17-21]. In the following, we limit ourselves to the hydrodynamic regime [22] which pertains to the long wavelength limit defined above, and to measurement times long compared to the time scale τ_I for direct (non-hydrodynamic) interactions. As suggested in Ref. [23] we identify τ_I with the mean time between protein collisions. According to Eq. (7.8.5) in Ref. [24] $\tau_I = (8\pi D_0 a n_p)^{-1}$, where the diffusivity D_0 is as defined below. At the lowest concentration $c_p = 2.5$ mg/ml, with the protein radius a ≈ 20Å and $D_0 = 11 \times 10^{-7}$ cm^2/s [15], we obtain $\tau_I = 1.8\text{x}10^{-6}$ s. For the measurement time we took the decay rate of the correlation function at the largest scattering angle, which is $\tau_D \approx 2\text{x}10^{-5}$ s. This is an order of magnitude larger than the collision time, and, thus, the above temporal constraint is fulfilled.

In this hydrodynamic regime, diffusivities derived from DLS represent the collective diffusion constant D_c [23, 25]. Including hydrodynamic interactions H(q) in the Oseen approximation, one can relate D_c to the solute properties in the form [22, 25, 26]

$$D_c = D_0 \frac{1 + H(q=0)}{S(q=0)}. \tag{5}$$

Here D_0 is the single particle diffusion constant obtained in the limit $c_p \rightarrow 0$, i.e., for vanishing protein-protein interactions. D_0 is related to the hydrodynamic particle radius a_h *via* the Stokes-Einstein relation

$$D_0 = \frac{k_B T}{6\pi \eta_0 a_h}, \tag{6}$$

where η_0 is the solvent viscosity. From Eqs. (1) and (5), one sees that both scattering intensity and diffusivity depend on direct interactions *via* the static structure factor, while hydrodynamic or indirect interactions affect the diffusivity only.

The static structure factor $S(q=0)$ and the hydrodynamic interaction term $H(q=0)$ can be related to a microscopic interaction potential $W(r)$ through the radial distribution function $g(r)$ [23]. In the dilute gas approximation, i.e. for sufficiently weak interactions [27]

$$g(r) \approx \exp\left[-\frac{W(r)}{k_B T}\right]. \tag{7}$$

In this approximation, linear expansions in terms of the solute volume fraction ϕ yield [14]

$$S(q=0,\phi) \approx 1 - k_S \phi, \quad H(q=0,\phi) \approx - k_H \phi \tag{8}$$

where the slope of the intensity data

$$k_S = 8 + 24 \int_0^\infty dx\, (1+x)^2 \{1 - \exp[-W(x)/k_B T]\} \tag{9}$$

and the slope of the hydrodynamic interactions

$$k_H = 6 + 12 \int_0^\infty dx\, F(x) \{1 - \exp[-W(x)/k_B T]\} \tag{10}$$

establish the connection with the interaction potential $W(x)$. The above $F(x) \approx 1 + x$ [14, 28] and the coordinate $x = r/2a - 1$ is the rescaled surface separation of two solute particles. Expressing Eq. (4) in terms of the volume fraction, using Eq. (8), one gets

$$\frac{Kc_p}{R_\theta} = \frac{1}{M}(1 + k_S \phi). \tag{11}$$

The corresponding linearizes form of Eq. (5) is then

$$D_c = D_0\left[1 + (k_S - k_H)\phi\right] \equiv D_0\left[1 + k_D \phi\right]. \tag{12}$$

II. EXPERIMENTS, DATA PRESENTATION AND EVALUATION

Hen egg white lysozyme is a globular protein of approximately ellipsoidal shape with two minor axis of 3.3 nm and a major axis of 5.5 nm diameter [15]. It is widely used as model system for protein crystal growth studies [29-31]. Prior to the light scattering experiments, we have analyzed lysozyme obtained from several commercial sources (Sigma, Boehringer-Mannheim and Seikagaku). SDS polyacrylamide gels, overloaded and silverstained, revealed various high molecular weight protein contaminants in all samples [32]. Six-times recrystallized and lyophilized Seikagaku had the least protein contaminants. It was used without further purification.

The protein was dissolved in two different solvents: 50 mM sodium acetate (NaAc) buffer at pH = 4.7 with sodium chloride added, or NaAc buffer alone ranging from 50 mM to 2.5 M in concentration. Most of the NaAc concentrations were chosen such that their respective ionic strength corresponds to one of the NaCl solutions used. The total ionic strength I is defined as

$$I = \frac{1}{2}\sum_i c_i z_i^2, \tag{13}$$

where the c_i are the concentrations of free ions of valence z_i. Thus, for the NaCl solutions, the ionic strength equals the molar NaCl concentration plus a small contribution from the 50mM NaAc buffer. For the NaAc solutions, we calculated I from the concentration of free ions in the pure NaAc buffer via the Henderson-Hasselbalch equation [33]. At pH = 4.7, the result is $[Na^+] \approx [Ac^-] \approx 0.47\times[\text{NaAc}]$. Due to the relatively low molar concentrations of the protein, its contribution to I and corresponding shifts in buffer ion concentration can be neglected, except, possibly, for $c_p > 50$ mg/ml in the 50mM NaAc solution.

Note that the above high NaAc concentrations cause a significant change in the solution viscosity. These must be corrected for in the data evaluation, as discussed below. Hence, we have measured kinematic viscosities and densities of the NaAc solutions with a Cannon-Ubbelohde capillary viscometer (size 50) and a standard pycnometer, respectively. The results are given in Table I. For the NaCl solutions we used the viscosity of the 50 mM NaAc buffer.

All chemicals used were reagent grade. Deionized water was used as solvent. For a given series of measurements, the precipitant concentration c_s was fixed and the protein concentration c_p was varied between 2.5 to 70 mg/ml. All solutions were filtered through Millipore Millex-Gv 0.22 μm syringe filters. To remove residual dust, and air bubbles introduced by filtration, the samples were centrifuged (Savant HSC10K at 9000 rpm) for 20 minutes. The pH of the final solutions was checked and remained at the pure buffer value within ±0.05. Only the 50 mM sodium acetate solutions showed a slight (≤ 0.15) but systematic pH increase at protein concentrations above 50 mg/ml, indicating that the solutions were somewhat under-buffered. Actual lysozyme concentrations were determined by UV-absorption measurements using $\alpha_{280} = 2.64$ ml/mg cm [34]. Protein concentrations were converted into volume fractions $\phi = \nu c_p$, using $\nu = 0.703$ ml/g for the specific volume of lysozyme [34].

The scattering cells consisted of borosilicate vials (10 mm ID) with stoppers. The cells were thoroughly cleaned with a cell washer (NSG Precision Cell) using a 1.5% tergazyme cleaning solution. After repeated rinses with deionized and filtered water the cells were vacuum dried and capped.

The light scattering set-up was as in Ref. [13] except for the use of an argon-ion laser ($\lambda = 514.5$ nm, light control mode, output power 80 mW). The sample temperature was maintained at T = 20±0.1 °C. All measurements were performed in vv-polarization at 10 different scattering angles θ between 30°-120°, with a typical measurement duration of 2 min/angle. The observed scattering volume of the goniometer varies with 1/sin(θ). Applying that correction resulted in angle-independent scattering intensities except for small glare contributions (<2%) at the two most forward angles. For given protein concentrations, we measured the scattering intensity and diffusivity at all angles. Before each measurement with a different protein concentration, absolute intensities were obtained through calibration with HPLC grade toluene. The toluene standard was filtered (0.1 μm) and sealed with a Teflon stopper under a nitrogen atmosphere. The Rayleigh ratio of toluene was taken as $R_{vv} = 23.8 \times 10^{-6}\ cm^{-1}$ (Table 2.1.1 in Ref. [19]). Rayleigh ratios of the protein solutions were determined for each scattering angle after subtracting

the background signal of the buffer/salt solution. Based on n_0 = 1.33 of water and an interpolated value for (dn/dc_p) of 0.227 ml/g, our instrument constant is K = 8.53×10^{-3} mol cm^2/g. For the (dn/dc_p) interpolation we used bracketing values given at 590 [35] and 488 nm [36].

IV. RESULTS AND DISCUSSION

Neither scattering intensities nor diffusivities revealed any angular dependence, confirming the above estimate that both, the form factor $P(q)$ and the static structure factor $S(q)$ assume the $q = 0$ limit in our systems. Hence, the measured Rayleigh ratios and diffusivities were averaged over all scattering angles, and the standard deviations were taken as measurement error. In addition, prior to nucleation, the data were time-independent. Nucleation lead to time- and angle-dependent increases first in scattering intensity, then in diffusivity.

The scattering intensity data for the various salt concentrations are presented in Figs. 1a and 1b as Debye plots of the scattering ratio Kc_p/R_θ *vs.* protein concentration c_p and corresponding volume fraction ϕ. One sees that in both precipitant systems Kc_p/R_θ follows the linear behavior expected from Eqs. (4) and (11). The straight lines in Figs. 1a and 1b represent least square fits to the data, with the intercepts at $c_p = 0$ yielding a molecular weight of approx. 13,600. This is below the published value of 14,600 [37]. The difference can be accounted for by uncertainties in both R_{vv} of toluene and (dn/dc_p), as well as small differences in observed scattering volume of the aqueous protein sample and the toluene standard.

From the slopes of the fitted lines in Figs. 1a and 1b, using Eq. (11), we obtained the values for k_S and corresponding B_2 listed in Table II. For the NaCl solutions, the virial coefficients agree well with data by Wilson [38]. The linearity of the Debye plots persists throughout the whole range of protein concentrations investigated, including supersaturated solutions (see full symbols in Fig. 1a). This validates George and Wilson's implicit assumption that B_2-values measured in undersaturated, low concentration solutions also characterize protein interactions in supersaturated solutions. Their correlation of slightly negative B_2 values to crystallization conditions is also confirmed for our supersaturated solutions.

The diffusivities obtained from single-exponential fits to the correlation data at the various salt concentrations are plotted in Figs. 2a and 2b *vs.* c_p. A second-order cumulant analysis [39] yielded D_c values which were only a few percent higher than the single exponential fits. The corresponding polydispersities were less than 0.03. Hence, the error in D_c introduced by the single-exponential fit is negligible. Note that, at the lowest salt concentrations in NaAc, the D_c curves show pronounced nonlinearities. At the highest salt concentrations, the nonlinearities are only weak. For intermediate ionic strengths the linear behavior expected from Eq.(12) persists out to the highest protein concentrations. The nonlinear behavior of the diffusivities indicates that protein transport is more sensitive to multi-body interactions than the scattering intensity. Linear interaction theory accounts for two-body interactions only. From fits to the linear range of the data according to Eq. (12), we obtained the values for k_D listed in Table II.

Note that in the NaAc solutions the D_0 values are shifted to lower values with increasing c_s. On correction for the increasing viscosity η_s (see Table I) in Eq. (6), however, all values fell within 3% of each other. The resulting $D_0 = 11.1 \times 10^{-7}$ cm^2/s is identical to that obtained in the NaCl-solutions, and slightly larger than the often referred to $D_0 = 10.6 \times 10^{-7}$ cm^2/s [15]. This higher value likely reflects the higher purity of our starting material. Using the above D_0 and $\eta_s = 1.014$ cp, the hydrodynamic radius obtained from Eq. (6) is $a_h = 1.9$ nm.

Several of the 2.5 M NaAc solutions nucleated during the measurements (see full symbols in Fig. 2b). Under these conditions, the measured diffusivities represent average values for the nuclei and the unaggregated solute [40]. The corresponding intensities fluctuated widely and were not included in Fig.1a. These fluctuations were due to the opposing effects of absorption and enhanced scattering by the nuclei.

Two of the supersaturated solutions did not nucleate during the measurements. Their diffusivities follow the linear concentration dependence of the undersaturated solutions (see the dashed line in Fig. 2b). This indicates that nucleation in lysozyme solutions follows the classical mechanism [41]: there are no intrinsic changes in the solution properties on transition from the undersaturated to the supersaturated state, until random clustering results in a critical nucleus that

can grow. Random clustering occurs at all protein concentrations independent of supersaturation. Its frequency (probability for collisions), however, increases with protein concentration and decreasing repulsion [42].

The slopes of the static and dynamic data, k_S and k_D (see also Table II), show two trends. Both change from large positive to negative values with increasing ionic strength of the solution. As expected $k_S > k_D$ for any given salt concentration, since, according to Eq. (12), k_D is decreased by the hydrodynamic interaction term k_H. Furthermore, at the same ionic strength, the values of k_S and k_D for the NaAc and NaCl solutions differ. This indicates that the changes are not a function of the ionic strength alone, but are salt specific.

The contributions of the hydrodynamic and direct interactions, *H(q=0)* and *S(q=0)*, to the diffusivity can be separated. Rewriting of Eq. (5) with Eq. (1) yields

$$1 + H(0) = \frac{D_c}{D_0} S(0) = \frac{D_c}{D_0 M} \left(\frac{Kc_p}{R_\theta} \right)^{-1} . \qquad (14)$$

The r.h.s. of Eq. (14) can be evaluated by combining static and dynamic data. The resulting plots of (1 + H(q=0)) *vs.* c_p for the two types of solutions are shown in Figs. 3a and 3b. Despite the scatter in the data (from combined errors of two data sets), one sees an increase in hydrodynamic interactions with increasing c_p as well as a pronounced decrease with increasing salt content. The increase with protein concentration is expected since the momentum transfer between the solute particles is enhanced upon reduction of the mean separation. However, the decrease with increasing c_s, to our knowledge, has not been observed before. Nevertheless, this dependence can be understood within the framework of the linear interaction model. We will expand on this point in the next section.

So far we have not considered possible solute aggregation as cause of the salt-induced changes in light scattering. However, several features in our data clearly indicate that these changes originate from those in protein interaction and not from aggregation. Specifically, the positive slopes in both Kc_p/R_θ and D_c *vs.* c_p, the linear dependence of Kc_p/R_θ on protein concentration [43], and the small and constant polydispersities [39] under all solution conditions

provide such evidence. It should be noted that our interpretation in terms of changing interactions is contrary to various recent aggregation models of protein crystallization [12, 30, 44, 45]. We will expand on this issue in a forthcoming publication [39].

V. COLLOIDAL INTERACTION MODEL

In order to provide some microscopic underpinning to our macroscopic observations, we have, similar to earlier work [3, 46-48], modeled the ionic strength dependence of k_S and k_D in terms of DLVO pair potentials for colloidal interactions [24]. In this model, the like charges Ze on the polyions provide the electrostatic repulsion. This repulsion is screened by a diffuse layer of thermally agitated counterions, that is treated within the framework of the Poisson-Boltzmann equation. The resulting exponential decrease in counterion concentration with distance from the polyion surface is characterized by the Debye-Hückel screening length λ_{DH}. Its inverse, the screening wave number $\kappa = 1/\lambda_{DH}$, is related to the ionic strength of the solution *via* [24]

$$\kappa = \sqrt{\frac{2000 N_A e^2}{\varepsilon k_B T} I}. \tag{15}$$

For our experimental conditions (see Table II), the screening layers are fairly compact ($\kappa a > 1$). Then the solution of the Poisson-Boltzmann equation for two charged spheres can be approximated by [47]

$$\frac{W_{el}(x)}{k_B T} = \frac{W_0}{k_B T} \frac{\exp(-2\kappa a x)}{x+1}. \tag{16}$$

The constant W_0 is obtained from the protein charge using equations (4.2-4.6) in Ref. [47].

The attractive term in the DLVO potential accounts for van der Waals contributions. These dispersion- or induced-dipole/induced-dipole forces in a dielectric medium are given by [47]

$$\frac{W_{vw}(x)}{k_B T} = -\frac{A_H}{12 k_B T}\left[\frac{1}{(x+1)^2} + \frac{1}{x^2+2x} + 2\ln\left(\frac{x^2+2x}{(x+1)^2}\right)\right], \tag{17}$$

where A_H is the Hamaker constant. Fig. 4 presents curves for W_{el}, W_{vw} and the resulting DLVO potential $W(x) = W_{el} + W_{vw}$, calculated for the various κ-values of our NaCl solutions, using Z

and A_H values as obtained below. Note the singularity in W(x) as the surface separation approaches zero.

Inserting the above interaction potential into Eqs. (9) and (10), with Z and A_H as fitting parameters, we have performed least square fits to the experimental values of $k_S(\kappa)$ and $k_D(\kappa)$. Similar to Ref. [28], the singularity at $W(x=0)$ was circumvented by an arbitrary lower cut-off x_{cut}, envisioned as the thickness of the Stern layer that prevents an unrealistically close approach of the polyions. We assumed the size of a salt ion in solution, 0.18 nm [49], for the thickness of this layer. This yields x_{cut} = 0.05. The integrals were evaluated with a Romberg algorithm [50] between x_{cut} and $x \approx 20$. On increase of the upper integration limit to $x \approx 2{,}000$ the numerical results remained unchanged. The choice of the lower limit, however, had considerable impact on the result of the integration, in contrast to earlier observations [28]. Given that x_{cut} lies in the potential's steep fall-off region (see Fig. 4), the sensitivity to the choice of x_{cut} is not surprising. The integrations and least square fits were performed on a Macintosh 6100 PowerPC using the Igor data analysis software from WaveMetrics with custom macros.

The $k_S(\kappa)$ curves resulting from the above fits are shown in Fig. 5a, together with the experimental values listed in Table II. Despite small systematic deviations of the model curve for the NaAc solutions, the overall trend in the $k_S(\kappa)$ data is well reproduced. Fig. 5b displays the corresponding $k_D(\kappa)$ results. One set of curves represents direct fits to $k_D(\kappa)$, the other set was calculated with the fitting parameters for $k_S(\kappa)$. Again, the theoretical curves capture the general dependence of k_D on κ, despite the noticeable differences in fitting parameters for static and dynamic data. The quantitative agreement for separate fits of either the static or dynamic data is quite encouraging, as well. In fact, the protein charge of about Z = 11, obtained from the static data in both salt solutions, closely matches experimental titration results [51]. Also the values for the Hamaker constant of order k_BT are reasonable. In addition, the interaction model provides a natural explanation for the observed dependence of the hydrodynamic interaction term $1+H(q=0) \approx 1-k_H \phi$ on salt concentration revealed by Figs. 3a-b. Plots of k_H as a function of κ for the two different salts, as calculated from Eq. (10), are given in Fig. 6. Note that k_H decreases

with increasing salt screening, and, for NaCl, even changes sign. We envision this decrease to be the result of more correlated, collinear motions of the solute particles on decrease of net repulsion. This, in turn, reduces their hydrodynamic friction [52]. In view of their large scatter, we made no attempt to quantiatively fit the experimental data of Figs. 3a and 3b to the above salt dependence of $1+H(q=0)$.

Recently, other authors have modeled interaction effects of lysozyme in NaCl solutions of ionic strength and pH close to our experimental condition by dynamic light scattering [3]. Our data show qualitatively similar trends. Yet, their diffusion measurements displayed considerably smaller slopes k_D at comparable ionic strength. This difference might be related to the amount and type of impurities in various samples, particularly since the D_0 values in our study are consistently higher than in Ref. [3]. The clear nonlinearities in our diffusion data appear absent from their data, even though the measurements extended out to almost twice the protein concentrations used in our study. Their fitting result for $Z = 6.4$ and $A_H = 7.7\ k_BT$ are quite different from ours. Direct comparison, however, is not meaningful due to the difference in measured k_D values and the use of another approximation to the Poisson-Boltzmann equation.

In lieu of Eq. (16), we also employed the forms of the electrostatic repulsion W_{el} valid for $\kappa a \gg 1$, that were used in Refs. [3] and [28]. Fits based on these expressions lead to consistently poorer results, that is larger residual errors of the least squares fits. In addition, as shown in Table III, these approximations result in similar inconsistencies in protein charge and Hamaker constant obtained from static and dynamic data. Most recently a new approximation scheme was proposed with very good agreement to numerical solutions of the Poisson-Boltzmann equation [53], which might result in more realistic values for the fitting parameters.

As we have seen in Figs. 5a and 5b, the screening wave number, at which either k_D or k_S change sign, depends on the salt. This cannot be derived from a colloidal interaction model. Salt-specific effects could result from alteration in the propagation of the van der Waals interactions through the solvent medium, or from specific absorption of salt ions into the immobile Stern layer of the protein. Although such effects are not accounted for in the current DLVO model, it does not

devalue the model calculations per se. Alterations to the dielectric environment can be easily incorporated and, with realistic expressions for the interaction potential, the actual protein charge could be derived from the model fits as above.

Another problem in our analysis scheme is the use of the dilute gas approximation to the radial distribution function (see Eq. (7)), which requires $W(r) << k_BT$. Even though our cut-off eliminates the singularity of $W(x)$, particularly the curves at low salt concentration exhibit maxima in the integration range of several k_BT. This might explain some of the problems in obtaining simultaneous, quantitative fits to both static and dynamic data. Several authors have circumvented this shortcoming by applying the hypernetted chain approximation to obtain the radial distribution function [46,54]. But even then, they found that the static data followed the calculated values very well, while deviations in the diffusivities persisted. Some of these residual deviations might have been caused by coupled salt-protein diffusion [49, 54] which becomes important at the low salt levels used in these works. This, however, does not apply to our systems.

In concluding this section, let us address some general concerns about the applicability of colloidal interaction potential to protein solutions. Irrespective of the quest for the most accurate analytical expression in the $\kappa a \approx 1$ regime, the electrostatic repulsion term in the DLVO potential provides an accurate description of many aspects of the solution behavior. This has been demonstrated under low salt conditions, where electrostatic repulsion is the dominating force and appropriate analytical expressions are well established. Excellent agreement between theoretical calculations, based on the hydrated protein and adsorpted salt ions as the charged unit, and intensity measurements were obtained for bovine serum albumin [46] and micellar CTACL solutions [54]. In view of the nonuniform shape of and charge distribution on the protein surface [55], the adequacy of the above spherical symmetric potentials might be surprising. However, the rapid rotational motion of lysozyme in solution [15] justifies this approximation.

The attractive term, on the other hand, is more problematic. First of all, proteins are zwitterions with substantial permanent dipole moments not included in the above van der Waals potential. Other attractive, even though short-ranged, interactions are relevant as well, including

charge fluctuations [56], hydrophobic interactions and hydrogen bonding [57]. It is not obvious which ones are dominant in our system and how to include them properly. The pronounced differences of lysozyme behavior in NaCl or NaAc solutions of comparable ionic strength serve as reminder that interactions specific to the solvent phase need to be accounted for.

Finally, the shape of the colloidal interaction potential for dominating attraction is inconsistent with the finite solubility of lysozyme in the 427 mM NaCl solution. At low salt concentrations, the electrostatic repulsion present a kinetic energy barrier against aggregation. However, the DLVO potential for $\kappa = 2.20\ nm^{-1}$ (see Fig. 4), which corresponds to the above NaCl concentration, lacks such a barrier. Since κ is practically independent of the protein concentration, the absence of a barrier implies that the solutions should precipitate for all c_p values, which is not found experimentally.

VI. SUMMARY AND CONCLUSIONS

We found that both scattering intensities and diffusivities respond to changes in protein interactions with salt content and depend on the salt type. Salts modify the protein interactions in two ways. First, the repulsive interaction decreases with increasing salt concentration through diffusive screening of the protein charge. Numerous earlier static and dynamic light scattering studies of protein solutions have demonstrated this dependence [7, 46, 48, 58-65]. In the framework of the DLVO model, salt screening is a unique function of the ionic strength of the solution, irrespective of salt type. However, our measurements reveal an additional, salt-specific effect. This could result from specific adsorption of ions onto the protein surface, or modification of the dielectric constant of the solvent medium. Similarly, sensitivity to the specific ions in solutions has been observed for protein solubilities with a large variety of salts [66]. The virial coefficients for these salt ions reflect the same trend [38]. Overall, these observations emphasize the close connection between the light scattering behavior of protein interactions and protein crystallization conditions.

The microscopic DLVO model presented here allows for a quantitative comparison with the phenomenologically introduced intensity and diffusivity slopes k_S and k_D. From this comparison

we can draw several conclusion. First of all, the microscopic model, in spite of various unrealistic approximations, reproduces the light scattering data and their dependence on protein and salt concentrations surprisingly well. Obviously, this interaction model contains some essential physical ingredients: long range electrostatic repulsion, moderated by salt screening, combined with a short range attractive term. The fitted protein charge and Hamaker constant are of a reasonable magnitude. However, the significant dependence of these fitting parameters on the specific approximations to the electrostatic repulsion indicates that the absolute values need to be viewed with proper caution. Similar discrepancies between separate fits to static and dynamic data have been noticed and discussed by previous investigators [46,54].

In conclusion, our measurements highlight the wealth of information available from combined static and dynamic light scattering in protein solutions. Quantitative comparison of the macroscopic results with microscopic interaction models provides insight into the underlying mechanisms. The study of solute interaction with light scattering is currently the most revealing method for determining crystallization conditions in protein solutions.

VII. ACKNOWLEDGMENTS

It is our pleasure to acknowledge stimulating discussions with D. Cannell, A.A. Chernov, H.Z. Cummins, and D.A. Weitz. W.W. Wilson has generously shared numerous insights and results prior to their publication. This research has been supported by NASA (Grant # NAG8-950) and the State of Alabama through the Center for Microgravity and Materials Research at the University of Alabama in Huntsville.

REFERENCES

[1] M. Halwer, G.C. Nutting and B.A. Brice, J. Am. Chem Soc. **73**, 2786 (1951).

[2] H.Z. Cummins in , *Photon Correlation and Light Beating Spectroscopy* , edited by H.Z. Cummins and E.R. Pike (Plenum Press, New York, 1974) p.313 and references therein.

[3] W. Eberstein, Y. Georgalis and W. Saenger, J. Crystal Growth **143**, 71 (1994).

[4] A. George and W.W. Wilson, Acta Cryst. **D50**, 361 (1994).

[5] A.J. Malkin and A. McPherson, J. Crystal Growth **133**, 29 (1993).

[6] M. Skouri, B. Lorber, R. Giegé, J.-P. Munch and J.S. Candau, J. Crystal Growth, in print.

[7] G.D. Phillies, G. B. Benedek, and N.A. Mazer, J. Chem. Phys. **65**, 1883 (1976).

[8] S. Lafont, S. Veesler, J.P. Astier, and R. Boistelle, J. Crystal Growth **143**, 249 (1994).

[9] T.Azuma, K. Tsukamoto and I. Sunagawa, J. Crystal Growth **98**, 371 (1989).

[10] Z. Kam, H.B. Shore and G. Feher, J. Mol. Biol. **123**, 539 (1978).

[11] M.L. Pusey, J. Crystal Growth **110**, 60 (1991).

[12] Y. Georgalis, A. Zouni, W. Eberstein and W. Saenger, J. Crystal Growth **126**, 245 (1993).

[13] J.B. Bishop, W.J. Fredericks, S.B. Howard and T. Sawada, J. Crystal Growth **122**, 41 (1992).

[14] L. Magid in Wyn Brown, *Dynamic Light Scattering, The Method and Some Applications* (Oxford University Press, New York, 1993) p. 554.

[15] S.B. Dubin, N.A. Clark and G.B. Benedek, J. Chem. Phys. **54**, 5158 (1971).

[16] H. Yamakawa, *Modern Theory of Polymer Solutions* (Harper and Row, New York, 1971), ch. 26.

[17] B.J. Berne and R. Pecora, *Dynamic Light Scattering* (Wiley, New York, 1976).

[18] *Dynamic Light Scattering, The Method and Some Applications* , edited by W. Brown, (Oxford University Press, New York, 1993).

[19] B. Chu, *Laser Light Scattering. Basic Principle and Practice* (Academic Press, New York, 1971).

[20] K.S. Schmitz, *An Introduction to Dynamic Light Scattering by Macromolecules* (Academic Press, San Diego, 1990).

[21] *Dynamic Light Scattering. Applications of Photon Correlation Spectroscopy*, edited by R. Pecora (Plenum Press, New York, 1985).

[22] B.J. Ackerson, J. Chem. Phys **69**, 684 (1978).

[23] P.N. Pusey, in ref [21], p. 85.

[24] R.J. Hunter, *Foundations of Colloid Science,vol I* (Clarendon Press, Oxford, 1987) p. 332.

[25] B.J. Ackerson, J. Chem. Phys **64**, 242 (1976).

[26] L. Belloni, M. Difford and P. Turq, J. Phys. Lett. **46**, L207 (1985).

[27] D.L. Goldstein, *States of Matter* (Prentice Hall, Englewood Cliffs, 1975) p. 265.

[28] M Corti and V. Degiorgio, J. Phys. Chem. **85**, 711 (1981).

[29] P.G. Vekilov, L.A. Monaco, and F. Rosenberger, J. Crystal Growth **148**, 289 (1995).

[30] A. Nadarajah, E.L. Forsythe, and M.L. Pusey, J. Crystal Growth **151**, 163 (1995).

[31] S.D. Durbin and W.E. Carlson , J. Crystal Growth **122**, 71 (1992).

[32] P.G. Vekilov, L.A. Monaco, and F. Rosenberger, J. Crystal Growth, accepted.

[33] K.E. van Holde, *Physical Biochemistry* (Prentice Hall, Englewood Cliffs, 1985) p. 77.

[34] A.J. Sophianopoulos, C.K. Rhodes, D.N. Holcomb and K.E. van Holde, J. Biol. Chem. **237**, 1107 (1962).

[35] W.J. Fredericks, M.C. Hammond, S.B. Howard and F. Rosenberger, J. Crystal Growth **141**, 183 (1994).

[36] B. Guo and W.W. Wilson, private communication.

[37] L.K. Steinrauf, Acta Cryst **12**, 77 (1959).

[38] W.W. Wilson, private communication.

[39] M. Muschol and F. Rosenberger, in preparation.

[40] G.A. Casey and W.W. Wilson, J. Crystal Growth **122**, 95 (1992).

[41] *Nucleation*, edited by A.C. Zettelmoyer (Marcel Dekker, New York, 1969).

[42] R. Hogg, T.W. Healy, and D.W. Fuerstenau, Trans. Faraday Soc. **62**, 1638 (1966).

[43] C. Tanford, *Physical Chemistry of Macromolecules* (Wiley, New York, 1961), p. 203.

[44] W. Kadima, A. McPherson, M.F. Dunn, and F.A. Jurnak, Biophys. J. **57**, 125 (1990).

[45] F. Boué, F. Lefaucheux, M.C. Robert and I. Rosenman, J. Crystal Growth **133**, 246 (1993).

[46] D. Neal, G. Purich and D.S. Cannell, J. Chem. Phys. **80**, 3469 (1984).

[47] D.M. Petsev, N.D. Denkov and K. Nagayama, Chem. Phys. **175**, 265 (1993).

[48] W.H. Gallagher and C.K. Woodward, Biopol. **28**, 2001 (1989).

[49] L. Belloni and M. Difford, J. Phys. Lett. **46**, L1183 (1985).

[50] W.H. Press, B.P. Flannery, S.A. Teukolsky and W.T. Vetterlin, *Numerical Recipes*, (Cambridge Univ. Press, New York, 1986).

[51] C. Tanford and M.L. Wagner, J. Am. Chem. Soc. **76**, 3331 (1954).

[52] D. Langbein, Adv. Colloid Interf. Sci. **46**, 91 (1993).

[53] J.E. Sader, S.L. Carnie, and D.Y. Chan, J. Colloid Int. Sci. **171**, 46 (1995).

[54] F. Ortega, R. Bacaloglu, D.C. McKenzie, C.A. Bunton and D.F. Nicoli, J. Phys. Chem. **94**, 501 (1990).

[55] B. Honig and A. Nicholls, Science **268**, 1144 (1995).

[56] J.G. Kirkwood and J.B. Shumaker, Proc. Nat. Acad. Sci., U.S., **38**, 863 (1952).

[57] J.N. Israelachvili, *Intermolecular and Surface Forces*,(Academic Press, London, 1991).

[58] P. Doty and R.F. Steiner, J. Chem. Phys. **20**, 85 (1952).

[59] T. Raj and W.H. Flygare, Biochem. **13**, 3336 (1974).

[60] J.L. Anderson and C.C. Reed, J. Chem. Phys. **64**, 3240 (1976).

[61] S.S. Alpert andG. Banks, Biophys. Chem. **4**, 287 (1976).

[62] J.L. Anderson, F. Rauh and A. Morales, J. Phys. Chem. **82**, 608 (1978).

[63] A.P. Minton and P.D. Ross, J. Phys. Chem. **82**, 1934 (1978).

[64] K.J. LaGattuta, V.S. Sharma, D.F. Nicoli and B.K. Koharti, Biophys. J. **33**, 63 (1981).

[65] B. Nyström and Robert M. Johnson, Chem. Scr. **22**, 82 (1982).

[66] M.M. Ries-Kautt and A.F. Ducruix, J. Biol. Chem. **264**, 745 (1989).

[67] F. Rosenberger, S.B. Howard, J.W. Soyers and T.A. Nyce,
J. Crystal Growth **129**, 1 (1993).

FIGURE CAPTIONS

Fig.1. Scattering ratio Kc_p/R_θ *vs.* protein concentration c_p in (a) 50mM sodium acetate (NaAc) buffer with added NaCL and (b) NaAc buffer at various concentrations. Identical symbols in (a) and (b) indicate comparable ionic strength of the solutions. Full symbols indicate supersaturation (see Ref. [67]). Typical error bars are comparable to or smaller than the symbol sizes. The straight lines are least squares fit to Eqn. (11). The fitting results for k_S are listed in Table II.

Fig. 2. Diffusivities D_c vs. lysozyme concentration c_p in (a) 50 mM sodium acetate (NaAc) buffer with added NaCl and (b) NaAc buffer at various concentration. Full symbols indicate nucleation events (instead of supersaturation as in Fig.1). The straight lines are fits to Eq. (12), with the corresponding result for k_D listed in Table II.

Fig. 3. Hydrodynamic interaction $1+H(q=0)$ *vs.* lysozyme concentration c_p in (a) 50 mM sodium acetate (NaAc) buffer with added NaCl and (b) NaAc buffer of various concentration. Connecting lines are added as visual guides only.

Fig. 4. DLVO pair interaction potential $W(x)$ as function of surface separation x. Dashed curve: attractive van der Waals term $W_{vw}(x)$ of Eq. (17). Thin solid curves: electrostatic repulsion $W_{el}(x)$ from Eq. (16) at the screening wave numbers κ corresponding to the NaCl solutions in Table II. Thick solid curves: total interaction potential $W(x)$. Values for the protein radius a = 1.9 nm, protein charge Z = 10.7 and Hamaker constant $A_H = 7.7\ k_BT$ were obtained from fits with NaCl solutions The shaded region indicates the cut-off below x = 0.05 used in the numerical integrations.

Fig. 5. Experimental values of (a) intensity slope k_S and (b) diffusivity slope k_D*vs.* screening wavenumber κ for NaCl and NaAc solutions. Thick curves: direct least squares fits to the experimental data for (a) $k_S(\kappa)$ and (b) $k_D(\kappa)$. Thin curves: theoretical $k_D(\kappa)$ obtained with the protein charge Z and Hamaker constant A_H resulting from fits to the $k_S(\kappa)$ data.

Fig. 6. Theoretical $k_H(\kappa)$ curves obtained with the protein charge Z and Hamaker constant A_H from fits to the $k_S(\kappa)$ data.

TABLE I. Density and kinematic viscosity of aqueous NaAc solutions measured at T = 20° C, and resulting dynamic viscosity values

c_s [mM]	$\Delta\rho/\rho_0$ x 10^3	ν [cSt]	η [cp]
0	0	1.004	1.002
50	1.6	1.014	1.014
100	2.7	1.028	1.029
250	6.3	1.057	1.061
375	9.3	1.085	1.093
920	22.4	1.199	1.224
1470	34.9	1.331	1.375
2500	59.2	1.654	1.749

TABLE II. Virial coefficient B_2, intensity slope k_S and diffusivity slope k_D of lysozyme at various ionic strengths I of NaCl and NaAc solutions.

	c_s [mM]	I [mM]	κ [nm^{-1}]	B_2 [10^{-4} mol ml /g^2]	k_S	k_D
NaCl	0	23[a]	0.50	16.8	69.8	33.1
	92	115[a]	1.11	2.8	11.7	0.8
	171	194[a]	1.45	0.7	2.7	-3.8
	427	450[a]	2.20	-2.1	-8.7	-12.1
NaAc	50	23	0.50	16.8	69.8	33.1
	100	47	0.71	10.5	43.9	16.4
	250	116	1.11	5.1	21.3	1.2
	375	174	1.37	3.8	15.9	-0.4
	920	428	2.15	1.1	4.6	-6.0
	1470	684	2.71	0.0	-0.17	-7.4

[a] Ionic strength of 50 mM NaAc buffer solution added

TABLE III. Protein charge Z and Hamaker constant A_H obtained from fits to the intensity slope $k_S(\kappa)$ or diffusivity slope $k_D(\kappa)$ for different approximations to the electrostatic interaction potential $W_{el}(x)$.

		$k_S(\kappa)$		$k_D(\kappa)$	
		NaCl	NaAc	NaCl	NaAc
$W_{el}(x)$	Z	10.7	10.9	8.5	8.6
Eq. (16)	A_H	8.1	4.3	8.5	7.2
$W_{el}(x)$ from	Z	6.5	6.5	5.4	5.4
Ref. [3]	A_H	6.3	2.7	7.2	6.0
$W_{el}(x)$ from	Z	3.9	3.9	3.1	3.2
Ref. [46]	A_H	5.2	1.5	6.4	5.1

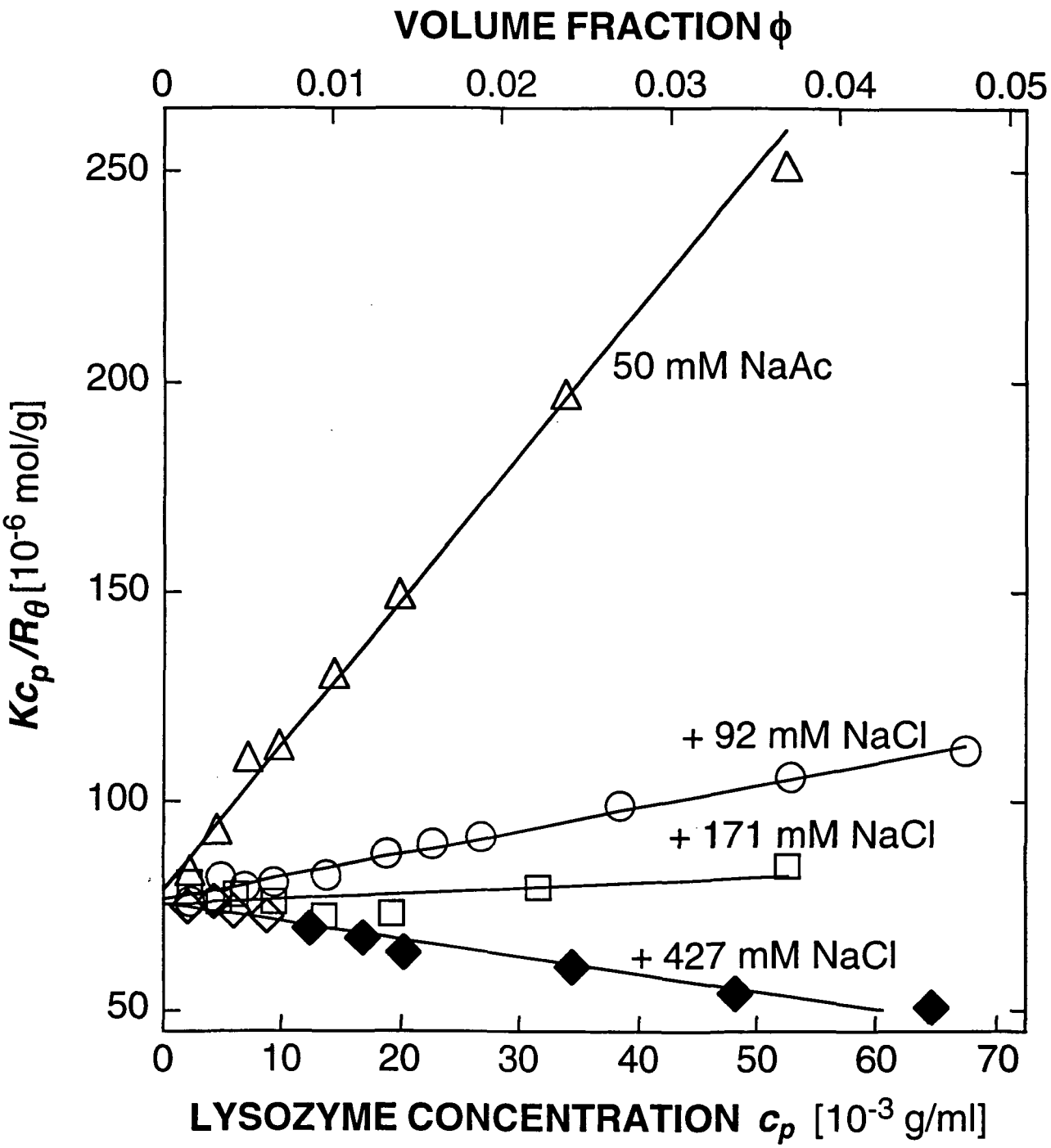
VOLUME FRACTION ϕ
0
0.01
0.02
0.03
0.04
0.05
250
200
150
100
50
Kc_p/R_θ [10^{-6} mol/g]
50 mM NaAc
+ 92 mM NaCl
+ 171 mM NaCl
+ 427 mM NaCl
0
10
20
30
40
50
60
70
LYSOZYME CONCENTRATION c_p [10^{-3} g/ml]

FIG. 1a

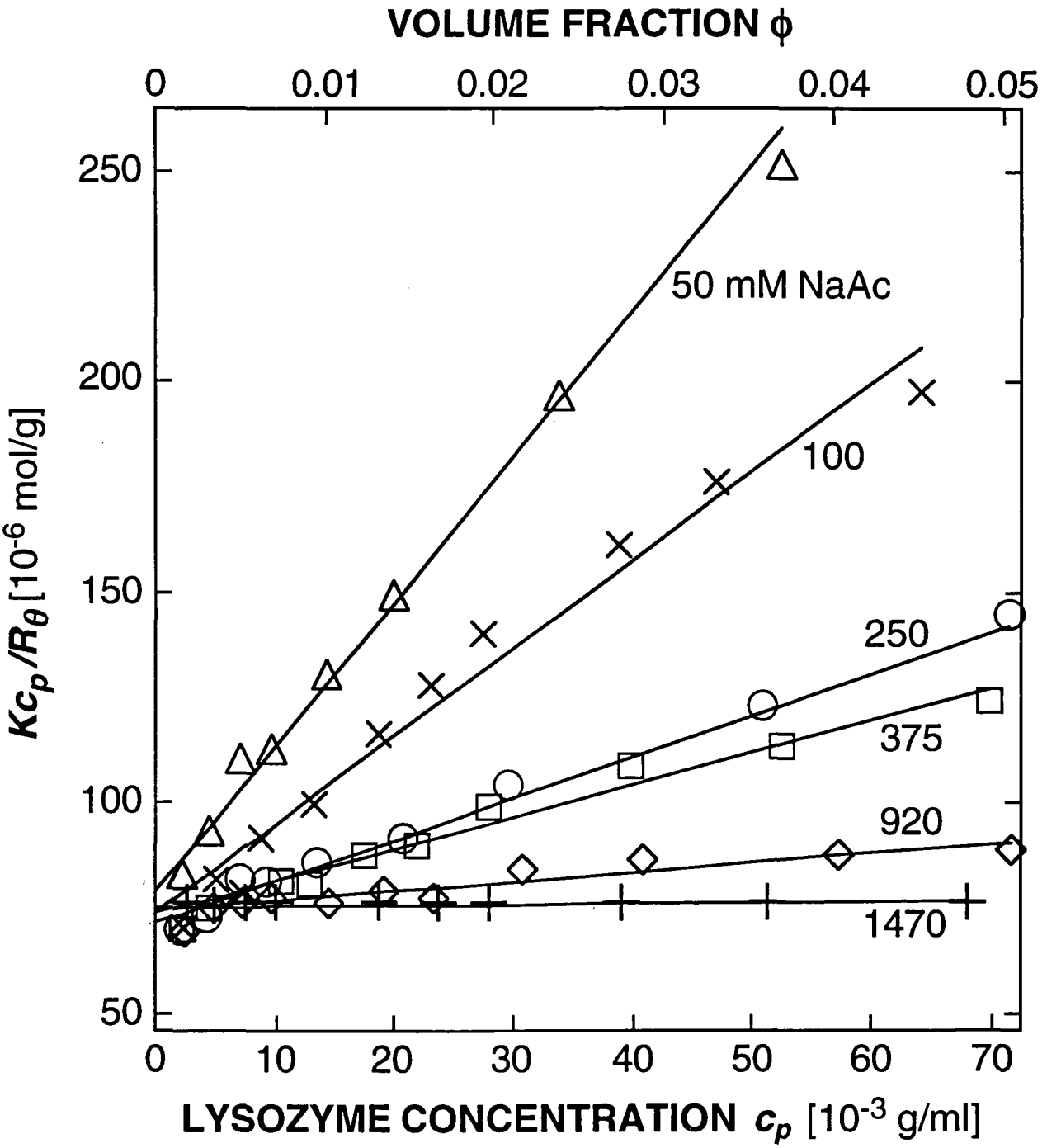
VOLUME FRACTION ϕ
0
0.01
0.02
0.03
0.04
0.05
250
200
150
100
50
Kc_p/R_θ [10^{-6} mol/g]
50 mM NaAc
100
250
375
920
1470
0
10
20
30
40
50
60
70
LYSOZYME CONCENTRATION c_p [10^{-3} g/ml]

FIG. 1b

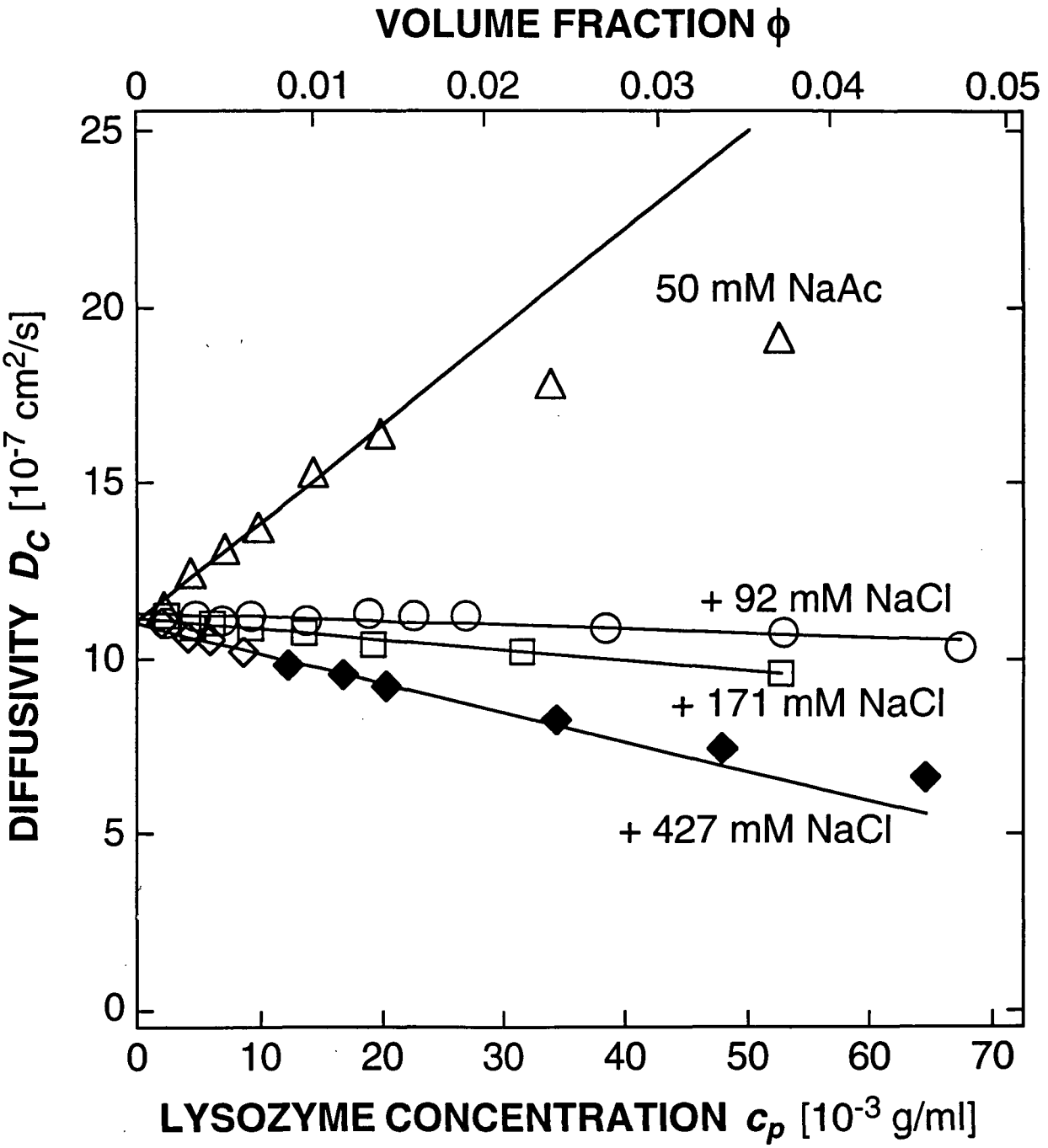
VOLUME FRACTION ϕ
0
0.01
0.02
0.03
0.04
0.05
25
20
15
10
5
0
DIFFUSIVITY D_C [10^{-7} cm^2/s]
50 mM NaAc
+ 92 mM NaCl
+ 171 mM NaCl
+ 427 mM NaCl
0
10
20
30
40
50
60
70
LYSOZYME CONCENTRATION c_p [10^{-3} g/ml]

FIG. 2a

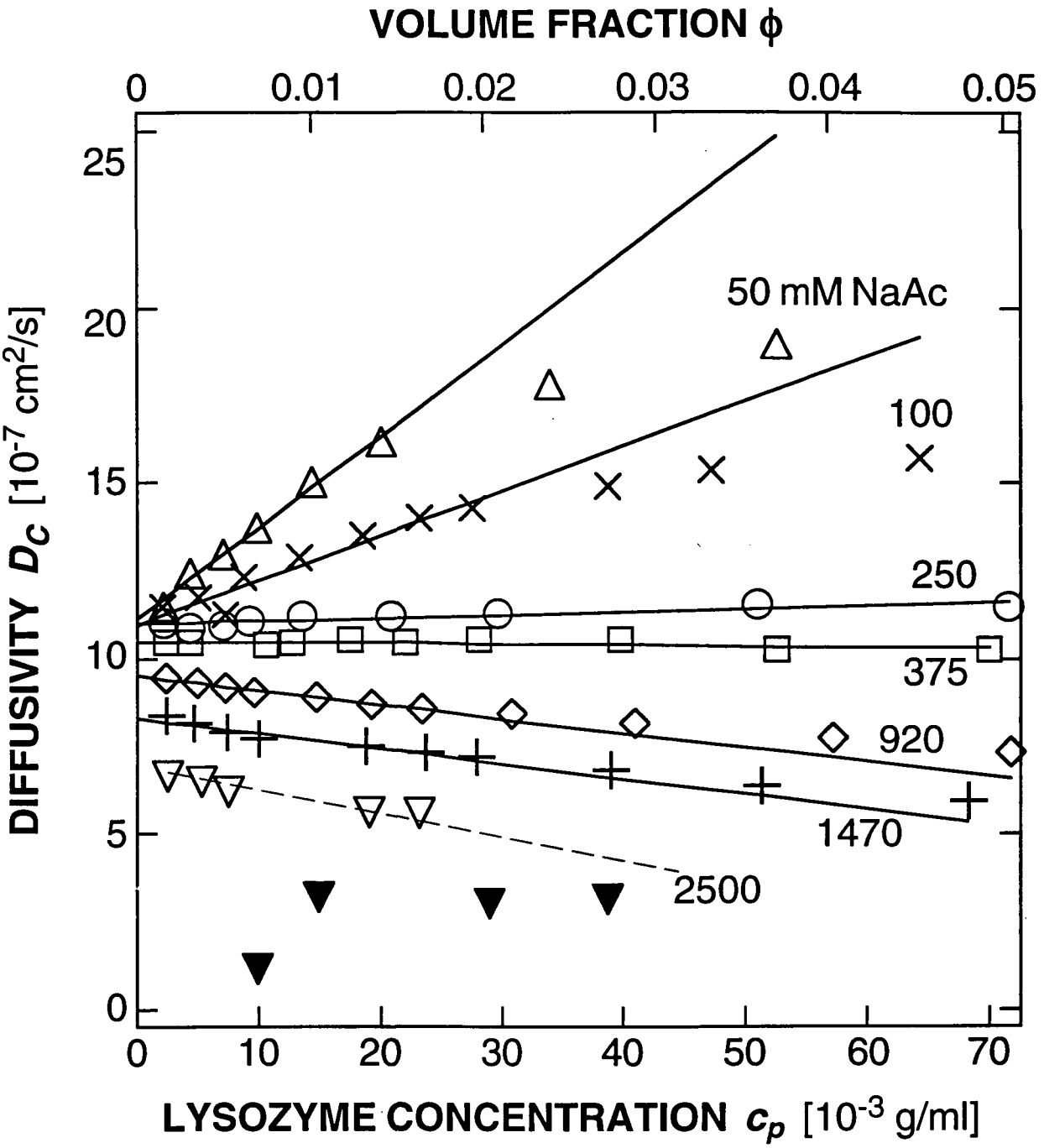
VOLUME FRACTION ϕ
0
0.01
0.02
0.03
0.04
0.05
25
20
15
10
5
0
DIFFUSIVITY D_C [10^{-7} cm^2/s]
50 mM NaAc
100
250
375
920
1470
2500
0
10
20
30
40
50
60
70
LYSOZYME CONCENTRATION c_p [10^{-3} g/ml]

FIG. 2b

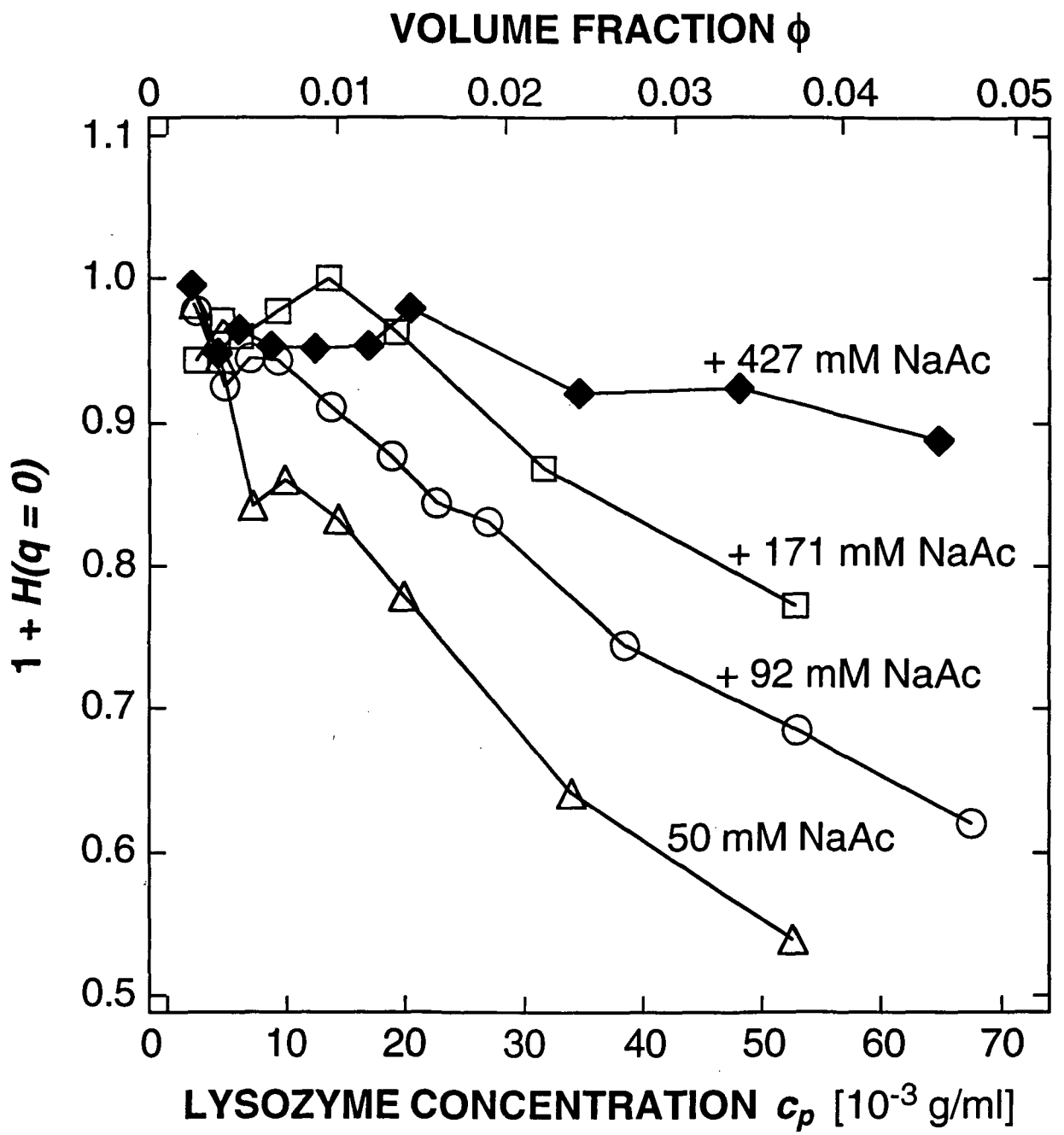
VOLUME FRACTION ϕ
0
0.01
0.02
0.03
0.04
0.05
1.1
1.0
0.9
0.8
0.7
0.6
0.5
1 + H(q = 0)
+ 427 mM NaAc
+ 171 mM NaAc
+ 92 mM NaAc
50 mM NaAc
0
10
20
30
40
50
60
70
LYSOZYME CONCENTRATION c_p [10^{-3} g/ml]

FIG. 3a

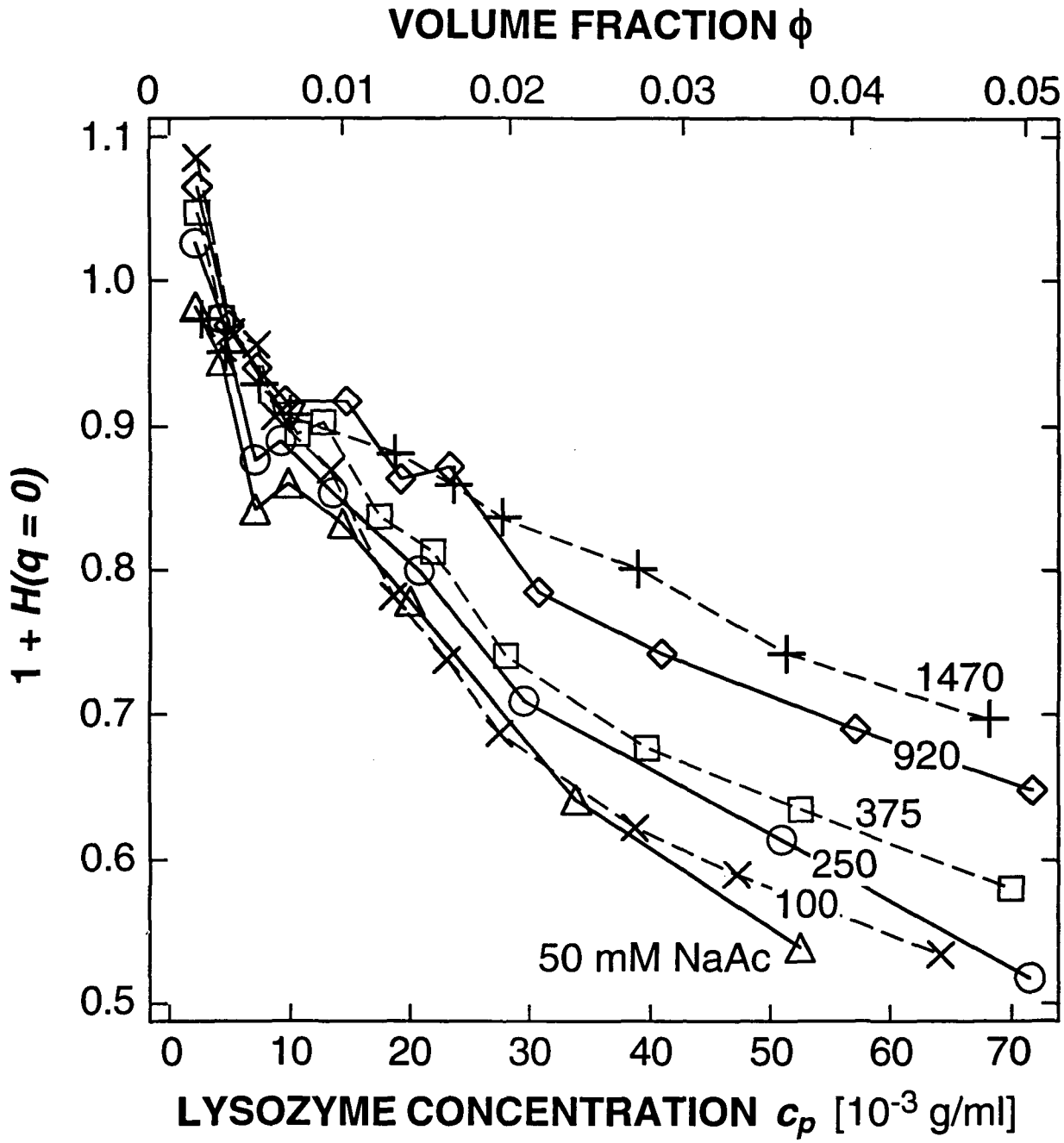
VOLUME FRACTION ϕ
0
0.01
0.02
0.03
0.04
0.05
1.1
1.0
0.9
0.8
0.7
0.6
0.5
1 + H(q = 0)
1470
920
375
250
100
50 mM NaAc
0
10
20
30
40
50
60
70
LYSOZYME CONCENTRATION c_p [10^{-3} g/ml]

FIG. 3b

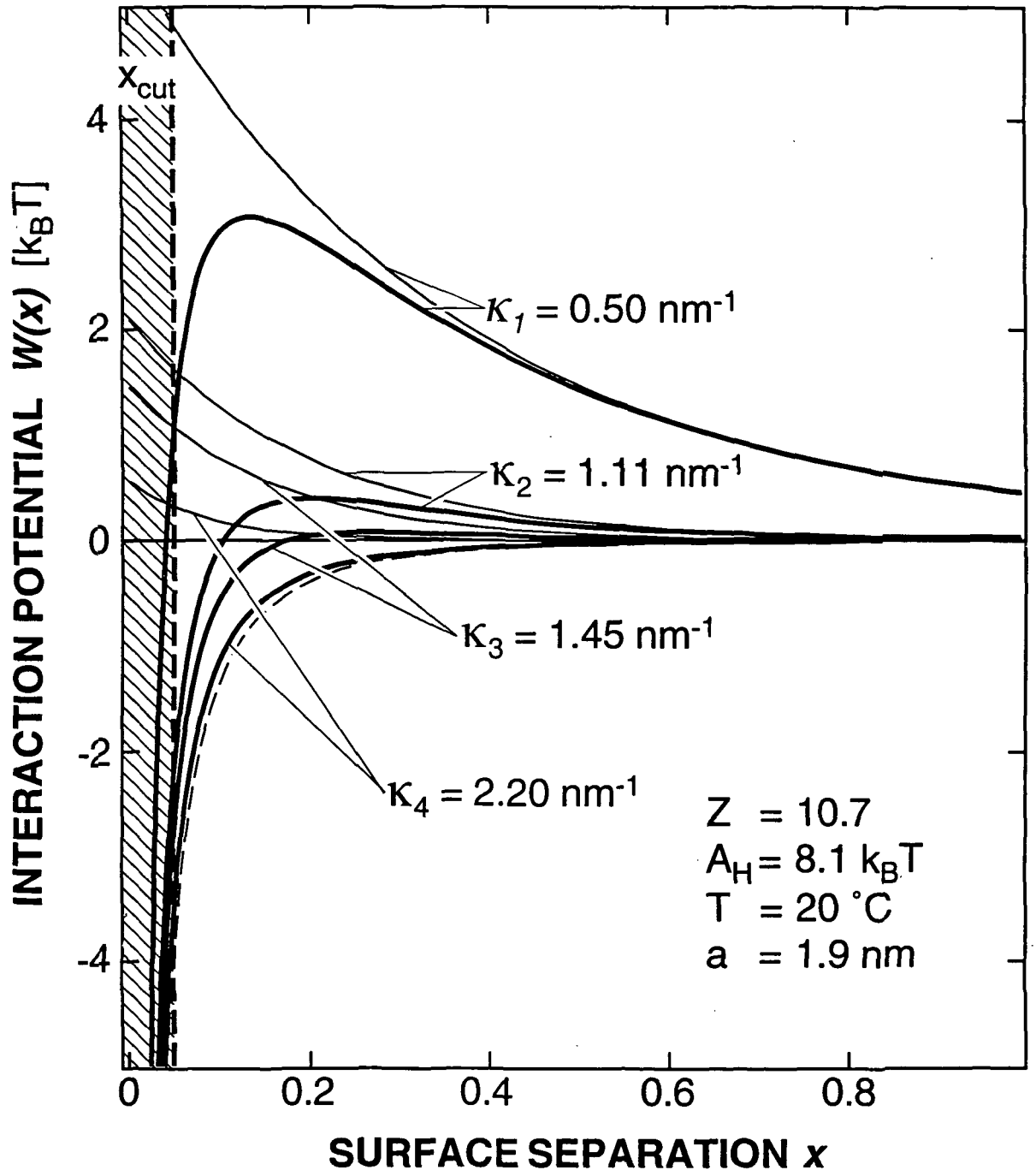
INTERACTION POTENTIAL W(x) [k_BT]
SURFACE SEPARATION x
x_cut
κ1 = 0.50 nm-1
κ2 = 1.11 nm-1
κ3 = 1.45 nm-1
κ4 = 2.20 nm-1
Z = 10.7
A_H = 8.1 k_BT
T = 20 °C
a = 1.9 nm
4
2
0
-2
-4
0
0.2
0.4
0.6
0.8

FIG. 4

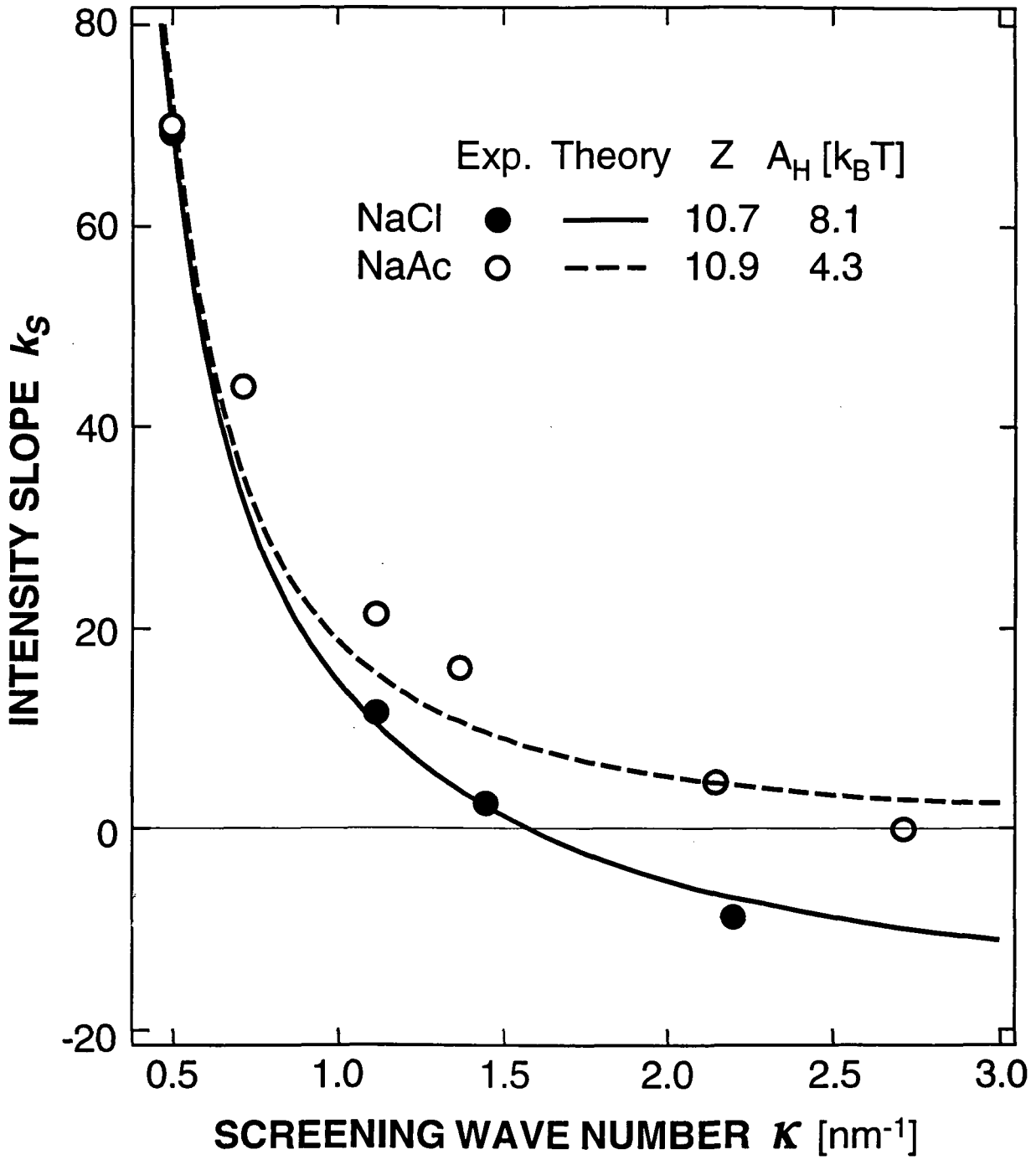
80
60
40
20
0
-20
0.5
1.0
1.5
2.0
2.5
3.0
INTENSITY SLOPE k_S
SCREENING WAVE NUMBER κ [nm^{-1}]
Exp. Theory Z A_H [k_BT]
NaCl ● —— 10.7 8.1
NaAc ○ - - - 10.9 4.3

FIG. 5a

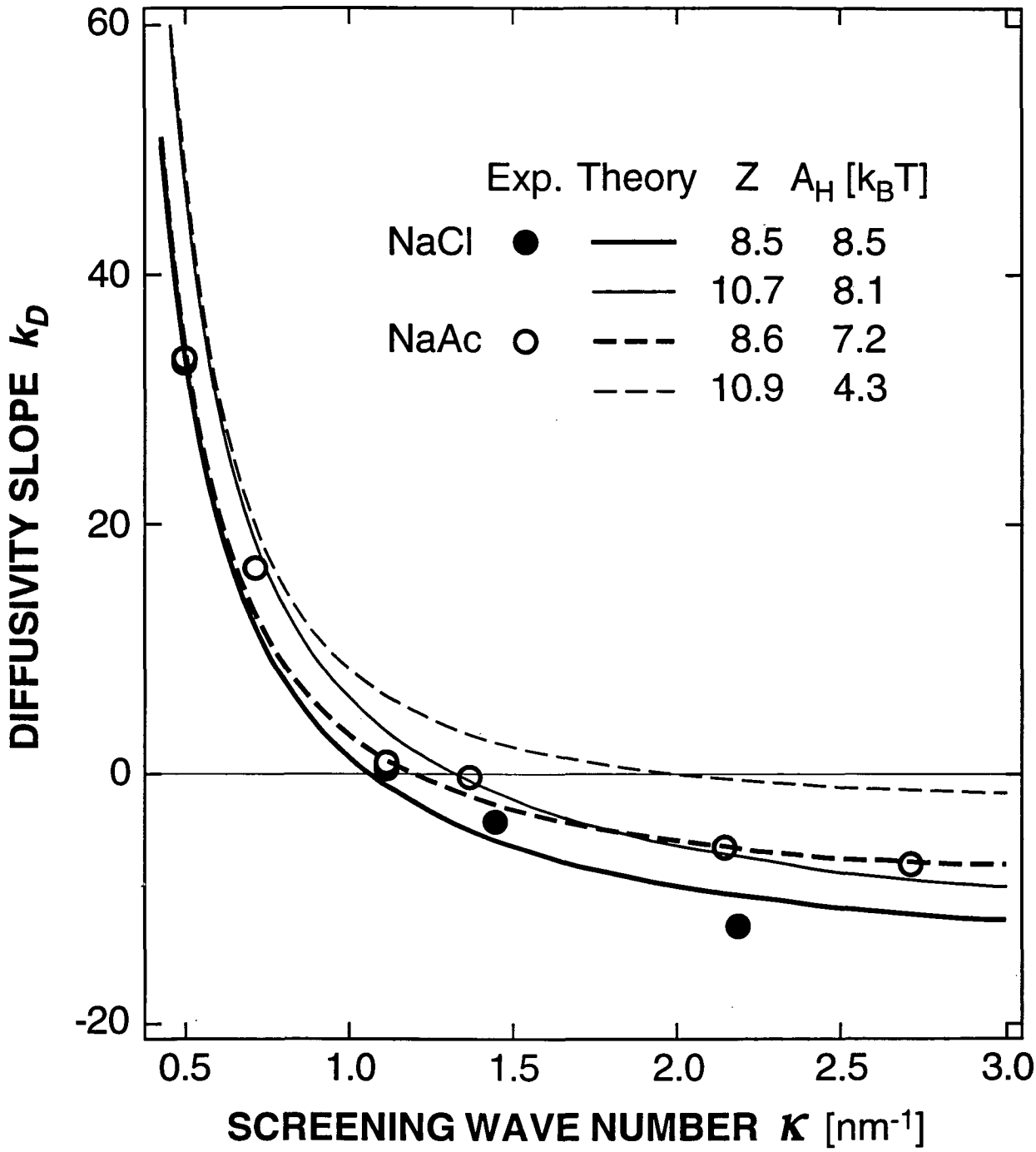
60
40
20
0
-20
0.5
1.0
1.5
2.0
2.5
3.0
DIFFUSIVITY SLOPE k_D
SCREENING WAVE NUMBER κ [nm^{-1}]
Exp. Theory Z A_H [k_BT]
NaCl 8.5 8.5
10.7 8.1
NaAc 8.6 7.2
10.9 4.3

FIG. 5b

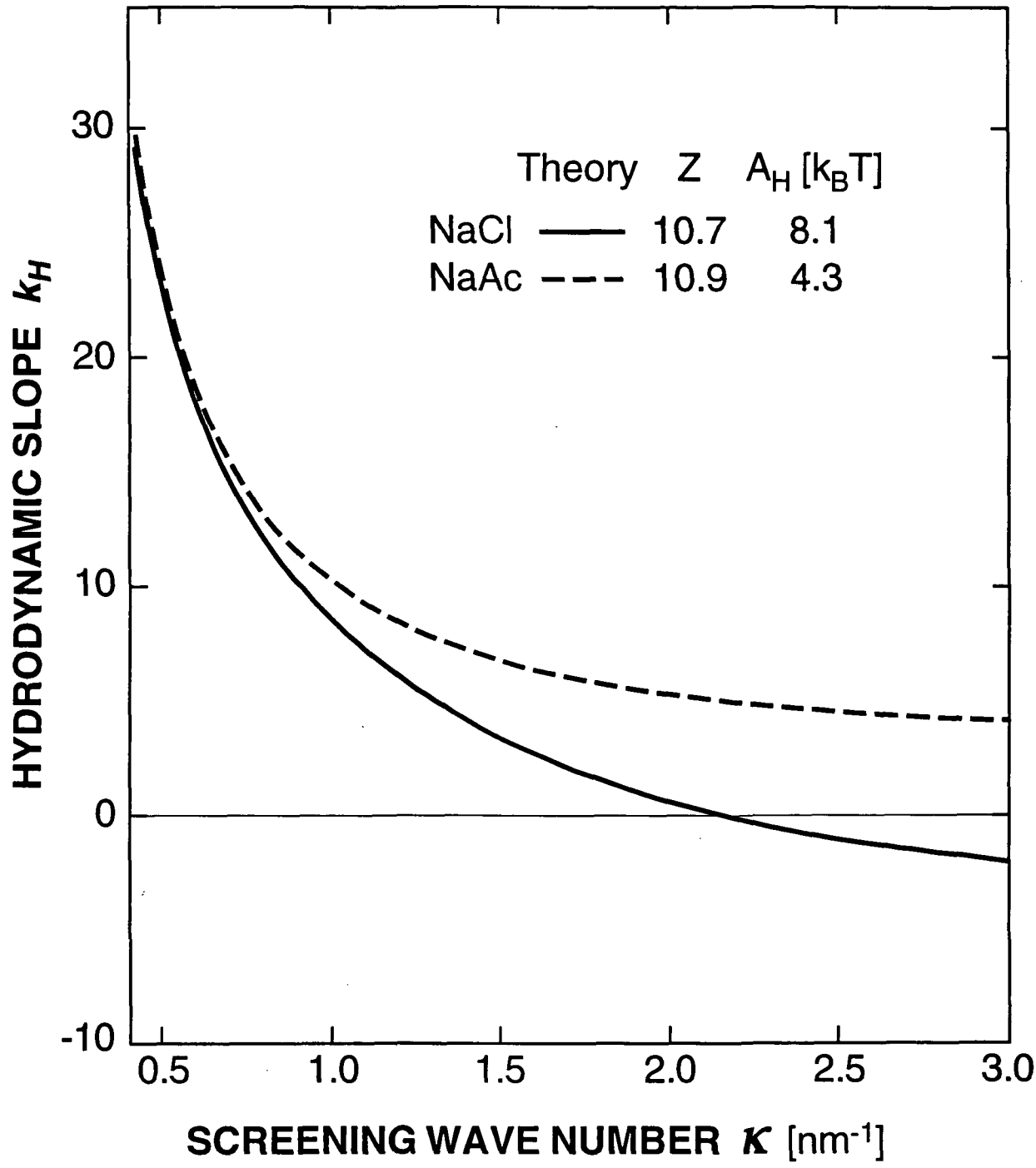
Theory Z A_H [k_BT]
NaCl 10.7 8.1
NaAc 10.9 4.3
HYDRODYNAMIC SLOPE k_H
30
20
10
0
-10
0.5
1.0
1.5
2.0
2.5
3.0
SCREENING WAVE NUMBER κ [nm^{-1}]

FIG. 6

Center for Microgravity and Materials Research
The University of Alabama in Huntsville